Phase-field modeling of the interactions between an edge dislocation and an array of obstacles

Shuozhi Xu[a,*], Justin Y. Cheng[b], Zezhou Li[b], Nathan A. Mara[b], Irene J. Beyerlein[a,c]

[a] *Department of Mechanical Engineering, University of California, Santa Barbara, CA 93106-5070, USA*
[b] *Department of Chemical Engineering and Materials Science, University of Minnesota, Minneapolis, MN 55455, USA*
[c] *Materials Department, University of California, Santa Barbara, CA 93106-5050, USA*

Abstract

Obstacles, such as voids and precipitates, are prevalent in crystalline materials. They strengthen crystals by serving as barriers to dislocation glide. In this work, we develop a phase-field dislocation dynamics (PFDD) technique for investigating the interactions between dislocations and second-phase obstacles, which can be either voids or precipitates. The PFDD technique is constructed to account for elastic heterogeneity, elastic anisotropy, dissociation of the dislocation, and dislocation transmission across bicrystalline interfaces. Within the framework, we present a model for "pseudo-voids", which are voids shearable by dislocations, in contrast to unphysical, unshearable voids in conventional phase-field dislocation formulations. We employ the PFDD technique to investigate the in-plane interactions between an edge dislocation and an array of nano-scale obstacles with different spacings. In this application, the interactions take place in glide planes of either a face-centered cubic (FCC) Cu or a body-centered cubic (BCC) Nb matrix, while the precipitates have a $Cu_{1-x}Nb_x$ composition, with x varying from 0.1 to 0.9. Our atomistic simulations find that the alloy precipitates can have an FCC, an amorphous, or a BCC phase, depending on the compositional ratio between Cu and Nb, i.e., value of x. Among all types of obstacles, the critical stresses for dislocation bypass are the highest for unshearable amorphous precipitates, followed by shearable crystalline precipitates, and then the pseudo-voids.

Keywords: Phase-field dislocation dynamics; Dislocation/obstacle interactions; Void; Precipitate

1. Introduction

Many strengthening methods for crystalline solids, such as irradiated materials [1,2], metal matrix composites [3,4], precipitate-hardened materials [5,6], and rapidly quenched metals [7], have been closely connected to dislocation/obstacle interactions at the nanoscale. In the grain interior, nano-sized obstacles dislocations can encounter, apart from other dislocations, can be classified as one of three types: voids, shearable precipitates, and unshearable precipitates. The interactions of dislocations and obstacles are intrinsically multi-scale due to the involvement of both long-range, linear elastic interactions and short-range, nonlinear atomic-scale ones [8,9].

Discrete models such as the atomistic simulation method [5,10,11] have been employed to account for these interactions.

While atomistic simulations have provided valuable insight on unit processes, they are ultimately limited in time and length scales, and hence in the obstacle sizes and dislocation numbers involved in the interactions. Continuum models, on the other hand, have the potential to achieve larger length scales. These methods include the coarse-grained atomistic approach [12,13], discrete dislocation dynamics (DDD) [14,15], level-set method [16,17], and generalized Peierls–Nabarro model [18]. To date, they can account for the long range stress fields and interaction energies between dislocations and other obstacles, e.g., precipitates, solutes, interstitial atoms, grain boundaries, and bi-material interfaces, while importing selected pieces of atomic-scale information for short-range interactions. Among these continuum models are those based on the phase-field (PF) method [19]. While originally developed to treat phase transformations, the formulation was adapted to simulate dislocation dynamics by defining a system energy model as a function of order parameters that are associated with dislocation slips [20,21].

Since its inception over twenty years ago [22], PF dislocation modeling has been employed to study a series of dislocation-mediated plastic problems in crystalline materials. A large body of studies have advanced the PF technique to better represent the properties of dislocations in a variety of material systems. In its most general form, the system energy includes an elastic energy for the long-range elastic field of a dislocation, a lattice energy for the short-range dislocation core field, and a gradient energy for the transitional regions between the two fields. Over the years, different choices have been made in terms of the model details, leading to a number of PF model variants. One popular PF dislocation model is the phase field microelasticity (PFM) model [22]. Using PFM for face-centered cubic (FCC) crystals, Shen and Wang [23] and Zheng et al. [24] modified the lattice energy term to better describe dislocation–dislocation interactions. In addition, Shen and Wang [25] incorporated the generalized stacking fault energy (GSFE) surfaces into the lattice energy to account for the dissociation of a dislocation to its equilibrium structure. Mianroodi and Svendsen [26] related the uniform gradient energy coefficient to the Shockley partial dislocation core size in FCC metals to yield better predictions of dissociated dislocations with respect to molecular statics simulations. Besides PFM, other PF dislocation models include the microscopic phase-field (MPF) model [27] and the phase-field dislocation dynamics (PFDD) model [28]. MPF confines all states of slip to pre-defined slip planes and excludes the gradient energy from its system energy. The original PFDD model did not include the gradient energy in its system energy either and assumed elastic isotropy for convenience. Recently, PFDD models were advanced for FCC crystals [29] by incorporating full anisotropic elasticity and the gradient energy, while separating the previously uniform gradient energy coefficient into two, one for the edge component and the other for the screw component. PFDD has also been extended to treat dislocations in body-centered cubic (BCC) [30,31] and hexagonal close-packed (HCP) materials [32,33]. All these methodological advancements in PFDD have enabled it to serve as a reliable tool for exploring dislocation dynamics in crystalline materials.

To date, PFDD has been applied to dislocations interacting with unshearable precipitates in FCC crystals [28,34], an incoherent twin boundary in Cu [35], and solutes in multi-principal element alloys (MPEAs) [36,37]. All these simulations assumed the material was elastically homogeneous. On the other hand, PFDD has also been applied to elastically heterogeneous bodies, i.e., dislocation evolution close to a void [38] and slip transfer of dislocations across bi-metal interfaces [39]. In these heterogeneous material treatments, however, other properties of the dislocations or materials, such as elastic anisotropy or dissociated dislocation cores, were not taken into account. To quantitatively assess the dislocation/obstacle interactions, which is the main goal of this paper, it is beneficial for PFDD to include all these features – material heterogeneities, dislocation dissociation, and anisotropic elasticity – into the same framework.

In this work, we present a unified PFDD technique that is capable of simulating in-plane interactions of dislocations with shearable or unshearable obstacles. We focus the investigation on the Cu–Nb system, wherein the matrix is either Cu or Nb while the obstacles are either voids or precipitates that are binary $Cu_{1-x}Nb_x$ alloys. We consider the full range of binary compositions, from precipitates with low concentrations of Nb that are FCC phases, to those with amorphous mixtures, and finally to larger concentrations of Nb that are BCC phases. The remainder of this paper is structured as follows. First, we introduce the PFDD formulation for an elastically homogeneous body in Section 2. Then in Section 3, we present the extension of PFDD to a two-phase elastic material. Last, in Sections 4, 5, and 6, the extended PFDD model is employed to study dislocation/obstacle interactions.

2. PFDD formulation in a homogeneous medium

In this section, we briefly review the PFDD formulation for an elastically homogeneous medium. We assume that the medium is a crystal that deforms elastically and plastically, where plasticity is accommodated by the glide of dislocations on preferred slip systems. An order parameter ϕ_α is introduced for each slip system α. The values $\phi_\alpha = 0$ and 1 represent the unslipped and slipped states, respectively. In the current work, ϕ_α is confined to be non-zero only in the slip plane of α [40], i.e., the dislocation core is assumed to not spread on multiple slip planes.

The total energy density ψ consists of three terms: elastic energy density ψ_{ela}, lattice energy density ψ_{lat}, and the external energy density ψ_{ext} [40], i.e.,

$$\psi(\boldsymbol{\epsilon}, \boldsymbol{\phi}) = \psi_{\text{ela}}(\boldsymbol{\epsilon}, \boldsymbol{\phi}) + \psi_{\text{lat}}(\boldsymbol{\phi}) - \psi_{\text{ext}}(\boldsymbol{\phi}) \tag{1}$$

where

$$\psi_{\text{ela}}(\boldsymbol{\epsilon}, \boldsymbol{\phi}) = \frac{1}{2}[\boldsymbol{\epsilon} - \boldsymbol{\epsilon}^{\text{p}}(\boldsymbol{\phi})] \cdot \boldsymbol{C}[\boldsymbol{\epsilon} - \boldsymbol{\epsilon}^{\text{p}}(\boldsymbol{\phi})] \tag{2}$$

$$\psi_{\text{lat}}(\boldsymbol{\phi}) = \frac{\gamma_{\text{gsf}}(\boldsymbol{\phi})}{l_{\text{gsf}}} \tag{3}$$

$$\psi_{\text{ext}}(\boldsymbol{\phi}) = \boldsymbol{\sigma}_{\text{app}} \cdot \boldsymbol{\epsilon}^{\text{p}}(\boldsymbol{\phi}) \tag{4}$$

where $\boldsymbol{C}$ is the elastic stiffness tensor, $\boldsymbol{\sigma}_{\text{app}}$ is the applied stress tensor, and $\boldsymbol{\phi}$ is the set of order parameters. The strain tensor field $\boldsymbol{\epsilon} = \text{sym } \boldsymbol{\beta}$, where $\boldsymbol{\beta} = \nabla \boldsymbol{u}$ is the distortion field with $\boldsymbol{u}$ being the displacement field. The plastic strain field $\boldsymbol{\epsilon}^{\text{p}} = \text{sym } \boldsymbol{\beta}^{\text{p}}$, where the plastic distortion $\boldsymbol{\beta}^{\text{p}}$ is related to the order parameters $\boldsymbol{\phi}$ by

$$\boldsymbol{\beta}^{\text{p}}(\boldsymbol{\phi}) = \sum_{\alpha=1}^{n_{\text{op}}} \frac{b_\alpha \phi_\alpha}{d_\alpha} \boldsymbol{s}_\alpha \otimes \boldsymbol{n}_\alpha \tag{5}$$

where $\boldsymbol{s}_\alpha$ is the slip direction unit vector, b_α is the slip vector magnitude, $\boldsymbol{n}_\alpha$ is the slip plane unit normal, and d_α is the interplanar spacing between two adjacent slip planes, for slip system α. n_{op} is the total number of order parameters.

The lattice energy density ψ_{lat} is associated with γ_{gsf}, the potential energy expense with shearing a crystalline half over the other half, while l_{gsf} is the spacing between the two halves. As a function of ϕ_α, γ_{gsf} is either an energy surface (when $n_{\text{sp}} > 1$) or an energy curve (when $n_{\text{sp}} = 1$), where n_{sp} is the number of order parameters per slip plane. In PFDD, γ_{gsf} is usually provided by atomistic simulations [30,41] or *ab initio* calculations [42,43].

Among edge and screw dislocations in nine FCC metals, our recent studies [29,40,43] found that, in most cases, if the gradient energy density was included in the master energy functional Eq. (1), it would yield a more accurate description of the dislocation core. However, the edge dislocation in Cu was a special case [43] because it was shown to be more beneficial to exclude the gradient energy density. In the meantime, the gradient energy density is usually not included for BCC metals [31]. Hence, the gradient energy density is not considered in this paper.

Once the energy functional is set and the order parameters are initialized, we minimize the total system energy with respect to each ϕ_α via the time-dependent Ginzburg–Landau (TDGL) equation, i.e.,

$$\dot{\phi}_\alpha = -m_0 \partial_{\phi_\alpha}(\psi_{\text{ela}} + \psi_{\text{lat}} - \psi_{\text{ext}}) \tag{6}$$

where the superposed dot denotes the time derivative and the Ginzburg–Landau coefficient m_0 is a non-negative constant.

3. Extension of PFDD to a heterogeneous medium

In this section, we present the PFDD formulation for a heterogeneous medium, which consists of two materials, respectively denoted by 1 and 2, with distinct anisotropic elasticity tensors $\boldsymbol{C}^{[1]}$ and $\boldsymbol{C}^{[2]}$. We can express $\psi_{\text{ela}}(\boldsymbol{x})$ (Eq. (2)) as a scalar field in $\boldsymbol{x}$, the position of a continuum point, i.e.,

$$\psi_{\text{ela}}(\boldsymbol{x}) = \frac{1}{2}C_{ijkl}(\boldsymbol{x})[\epsilon_{ij}(\boldsymbol{x}) - \epsilon_{ij}^{\text{p}}(\boldsymbol{x})][\epsilon_{kl}(\boldsymbol{x}) - \epsilon_{kl}^{\text{p}}(\boldsymbol{x})] \tag{7}$$

In the meantime, employing Hooke's Law to relate the stress tensor to elastic strain, we have

$$\sigma_{ij}(\boldsymbol{x}) = C_{ijkl}(\boldsymbol{x})[\epsilon_{kl}(\boldsymbol{x}) - \epsilon_{kl}^{\text{p}}(\boldsymbol{x})] \tag{8}$$

In an elastically homogeneous medium, $C_{ijkl}(\boldsymbol{x})$ is a constant everywhere, and so the total elastic energy can be calculated in the Fourier space, with the help of the Plancherel theorem [43]. In an elastically heterogeneous medium consisting of two materials, however, $C_{ijkl}(\boldsymbol{x})$ varies spatially, i.e.,

$$C_{ijkl}(\boldsymbol{x}) = \begin{cases} C_{ijkl}^{[1]}, & \boldsymbol{x} \in \text{material 1} \\ C_{ijkl}^{[2]}, & \boldsymbol{x} \in \text{material 2} \end{cases} \tag{9}$$

Due to the spatial variation of C_{ijkl}, calculating the total elastic energy becomes more difficult because the Plancherel theorem cannot be used directly. Eshelby [44] proposed that, if the strain caused by material 2 is uniform within itself and is zero in material 1, the elastic field of the two-material medium would be equivalent to adding a virtual strain $\boldsymbol{\epsilon}^{\text{v}}$ to material 2, while assuming a uniform elastic tensor $C_{ijkl}^{[1]}$ in both materials. It follows that the stress becomes

$$\sigma_{ij}(\boldsymbol{x}) = C_{ijkl}^{[1]}[\epsilon_{kl}(\boldsymbol{x}) - \epsilon_{kl}^0(\boldsymbol{x})] \tag{10}$$

where the eigenstrain (i.e., inelastic strain) is given by

$$\epsilon_{kl}^0(\boldsymbol{x}) = \begin{cases} \epsilon_{kl}^{\text{p}}(\boldsymbol{x}), & \boldsymbol{x} \in \text{material 1} \\ \epsilon_{kl}^{\text{p}}(\boldsymbol{x}) + \epsilon_{kl}^{\text{v}}(\boldsymbol{x}), & \boldsymbol{x} \in \text{material 2} \end{cases} \tag{11}$$

The virtual strain $\boldsymbol{\epsilon}^{\text{v}}$, which is zero in material 1 and non-zero in material 2, is defined such that Eqs. (8) and (10) equal each other. The equality is trivial in material 1. In material 2, however, their equality dictates that

$$C_{ijkl}^{[2]}[\epsilon_{kl}(\boldsymbol{x}) - \epsilon_{kl}^{\text{p}}(\boldsymbol{x})] = C_{ijkl}^{[1]}[\epsilon_{kl}(\boldsymbol{x}) - \epsilon_{kl}^{\text{p}}(\boldsymbol{x}) - \epsilon_{kl}^{\text{v}}(\boldsymbol{x})] \tag{12}$$

Equivalently

$$- C_{ijkl}^{[1]}\epsilon_{kl}^{\text{v}}(\boldsymbol{x}) = \Delta C_{ijkl}[\epsilon_{kl}(\boldsymbol{x}) - \epsilon_{kl}^{\text{p}}(\boldsymbol{x})] \tag{13}$$

where $\Delta C_{ijkl} = C_{ijkl}^{[2]} - C_{ijkl}^{[1]}$. Eq. (13) can be written in a more general form for both materials 1 and 2, i.e.,

$$C_{ijkl}^{[1]}\epsilon_{kl}^{\text{p}}(\boldsymbol{x}) = C_{ijkl}^{[1]}\epsilon_{kl}^0(\boldsymbol{x}) + \Delta C_{ijkl}(\boldsymbol{x})[\epsilon_{kl}(\boldsymbol{x}) - \epsilon_{kl}^{\text{p}}(\boldsymbol{x})] \tag{14}$$

where

$$\Delta C_{ijkl}(\boldsymbol{x}) = C_{ijkl}(\boldsymbol{x}) - C_{ijkl}^{[1]} \tag{15}$$

The elastic energy density $\psi_{\text{ela}}(\boldsymbol{x})$ can then be written as the sum of the "equivalent" homogeneous elastic energy density, $\psi_{\text{ela}}^{\text{eq}}(\boldsymbol{x})$, and the "extra" elastic energy density, $\psi_{\text{ela}}^{\text{ex}}(\boldsymbol{x})$, i.e.,

$$\psi_{\text{ela}}(\boldsymbol{x}) = \psi_{\text{ela}}^{\text{eq}}(\boldsymbol{x}) + \psi_{\text{ela}}^{\text{ex}}(\boldsymbol{x}) \tag{16}$$

where

$$\psi_{\text{ela}}^{\text{eq}}(\boldsymbol{x}) = \frac{1}{2}C_{ijkl}^{[1]}[\epsilon_{ij}(\boldsymbol{x}) - \epsilon_{ij}^0(\boldsymbol{x})][\epsilon_{kl}(\boldsymbol{x}) - \epsilon_{kl}^0(\boldsymbol{x})] \tag{17}$$

$$\psi_{\text{ela}}^{\text{ex}}(\boldsymbol{x}) = \frac{1}{2}M_{ijkl}(\boldsymbol{x})\epsilon_{ij}^{\text{v}}(\boldsymbol{x})\epsilon_{kl}^{\text{v}}(\boldsymbol{x}) \tag{18}$$

where

$$M_{ijkl}(\boldsymbol{x}) = -C_{ijmn}^{[1]}\left[\Delta C_{mnpq}(\boldsymbol{x})\right]^{-1}C_{pqkl}^{[1]} - C_{ijkl}^{[1]} \tag{19}$$

Derivation of Eq. (16) is presented in Appendix A. According to Eq. (11), $\epsilon_{kl}^{\text{v}}(\boldsymbol{x})$ is defined only in material 2, not in material 1. As a result, $\psi_{\text{ela}}^{\text{ex}}(\boldsymbol{x})$ is defined only in material 2.

Besides the elastic energy density, there are two other energy densities in Eq. (1). In the case of a heterogeneous medium, the lattice energy density does not change its form, while the external energy density should be slightly modified in material 2, from Eq. (4), to

$$\psi_{\text{ext}}(\boldsymbol{\phi}, \boldsymbol{\epsilon}^{\text{v}}) = \boldsymbol{\sigma}_{\text{app}} \cdot \boldsymbol{\epsilon}^0(\boldsymbol{\phi}, \boldsymbol{\epsilon}^{\text{v}}) \tag{20}$$

3.1. Dislocations are not permissible in material 2

In this section, we consider the case when dislocations are permissible in material 1 but not in material 2, e.g., when material 2 is unshearable and/or amorphous. Note that the dislocation slip is the only plastic deformation mechanism in PFDD; other plasticity mechanisms such as twinning (in crystals) and shear transformation zone (in amorphous materials) are not considered. In this case, $\boldsymbol{\phi}$ correspond to the order parameters only in material 1. It follows that, the eigenstrain becomes

$$\boldsymbol{\epsilon}^0(\boldsymbol{x}) = \begin{cases} \boldsymbol{\epsilon}^{\mathrm{p}}(\boldsymbol{\phi}(\boldsymbol{x})), & \boldsymbol{x} \in \text{material 1} \\ \boldsymbol{\epsilon}^{\mathrm{v}}(\boldsymbol{x}), & \boldsymbol{x} \in \text{material 2} \end{cases} \tag{21}$$

Therefore, the elastic energy density becomes

$$\psi_{\mathrm{ela}}(\boldsymbol{x}) = \begin{cases} \psi_{\mathrm{ela}}^{\mathrm{eq}}(\boldsymbol{\phi}(\boldsymbol{x})), & \boldsymbol{x} \in \text{material 1} \\ \psi_{\mathrm{ela}}^{\mathrm{ex}}(\boldsymbol{\epsilon}^{\mathrm{v}}(\boldsymbol{x})), & \boldsymbol{x} \in \text{material 2} \end{cases} \tag{22}$$

the lattice energy density becomes

$$\psi_{\mathrm{lat}}(\boldsymbol{x}) = \begin{cases} \dfrac{\gamma_{\mathrm{gsf}}^{[1]}(\boldsymbol{\phi}(\boldsymbol{x}))}{l_{\mathrm{gsf}}^{[1]}}, & \boldsymbol{x} \in \text{material 1} \\ 0, & \boldsymbol{x} \in \text{material 2} \end{cases} \tag{23}$$

and the external energy density becomes

$$\psi_{\mathrm{ext}}(\boldsymbol{x}) = \begin{cases} \boldsymbol{\sigma}_{\mathrm{app}} \cdot \boldsymbol{\epsilon}^{\mathrm{p}}(\boldsymbol{\phi}(\boldsymbol{x})), & \boldsymbol{x} \in \text{material 1} \\ \boldsymbol{\sigma}_{\mathrm{app}} \cdot \boldsymbol{\epsilon}^{\mathrm{v}}(\boldsymbol{x}), & \boldsymbol{x} \in \text{material 2} \end{cases} \tag{24}$$

Different from the homogeneous medium case, which uses Eq. (6), an additional set of TDGL equations is used here because the total energy should also be minimized with respect to each of the nine components of $\boldsymbol{\epsilon}^{\mathrm{v}}$, i.e.,

$$\dot{\phi}_\alpha = -m_0 \partial_{\phi_\alpha}(\psi_{\mathrm{ela}} + \psi_{\mathrm{lat}} - \psi_{\mathrm{ext}}) \quad \text{in material 1} \tag{25}$$

$$\dot{\epsilon}_{ab}^{\mathrm{v}} = -m_0^{\mathrm{v}} \partial_{\epsilon_{ab}^{\mathrm{v}}}(\psi_{\mathrm{ela}} - \psi_{\mathrm{ext}}) \quad \text{in material 2} \tag{26}$$

where $a, b = 1, 2, 3$. Note that the Ginzburg–Landau coefficients m_0 and m_0^{v} are not necessarily the same but should both be positive; the final equilibrium state is independent of the absolute values of these coefficients [39]. Also note that Eq. (26) minimizes the system energy only if $\left[\Delta C_{mnpq}\right]^{-1}$ is negative definite, i.e., when material 1 is stiffer than material 2 [45]. If $\left[\Delta C_{mnpq}\right]^{-1} > 0$, Eq. (26) will result in divergence of the virtual strain.

3.2. Dislocations are permissible in material 2

When both materials are crystalline and shearable by dislocations, each one has not only its own elastic moduli, but also its own lattice energy, lattice parameter, and set of order parameters. In the present model, we consider situations in which the mismatch between the two lattice constants are sufficiently low that the interface is coherent or semi-coherent, with negligible coherency strains. Materials 1 and 2 are also assumed to have the same lattice type and slip system. Using $\boldsymbol{\phi}$ and $\boldsymbol{\phi}^\dagger$ to denote the order parameter sets in materials 1 and 2, respectively, the elastic energy density becomes

$$\psi_{\mathrm{ela}}(\boldsymbol{x}) = \begin{cases} \psi_{\mathrm{ela}}^{\mathrm{eq}}(\boldsymbol{\phi}(\boldsymbol{x})), & \boldsymbol{x} \in \text{material 1} \\ \psi_{\mathrm{ela}}^{\mathrm{eq}}(\boldsymbol{\phi}^\dagger(\boldsymbol{x})) + \psi_{\mathrm{ela}}^{\mathrm{ex}}(\boldsymbol{\epsilon}^{\mathrm{v}}(\boldsymbol{x})), & \boldsymbol{x} \in \text{material 2} \end{cases} \tag{27}$$

where

$$\psi_{\mathrm{ela}}^{\mathrm{eq}}(\boldsymbol{x}) = \begin{cases} \dfrac{1}{2} C_{ijkl}^{[1]}[\epsilon_{ij}(\boldsymbol{x}) - \epsilon_{ij}^0(\boldsymbol{\phi}(\boldsymbol{x}))][\epsilon_{kl}(\boldsymbol{x}) - \epsilon_{kl}^0(\boldsymbol{\phi}(\boldsymbol{x}))], & \boldsymbol{x} \in \text{material 1} \\ \dfrac{1}{2} C_{ijkl}^{[1]}[\epsilon_{ij}(\boldsymbol{x}) - \epsilon_{ij}^0(\boldsymbol{\phi}^\dagger(\boldsymbol{x}))][\epsilon_{kl}(\boldsymbol{x}) - \epsilon_{kl}^0(\boldsymbol{\phi}^\dagger(\boldsymbol{x}))], & \boldsymbol{x} \in \text{material 2} \end{cases} \tag{28}$$

Similarly, the lattice energy density becomes

$$
\psi_{\mathrm{lat}}(\boldsymbol{x}) = \begin{cases} \dfrac{\gamma_{\mathrm{gsf}}^{[1]}(\boldsymbol{\phi}(\boldsymbol{x}))}{l_{\mathrm{gsf}}^{[1]}}, & \boldsymbol{x} \in \text{material 1} \\[4mm] \dfrac{\gamma_{\mathrm{gsf}}^{[2]}(\boldsymbol{\phi}^{\dagger}(\boldsymbol{x}))}{l_{\mathrm{gsf}}^{[2]}}, & \boldsymbol{x} \in \text{material 2} \end{cases}
\tag{29}
$$

and the external energy density becomes

$$
\psi_{\mathrm{ext}}(\boldsymbol{x}) = \begin{cases} \boldsymbol{\sigma}_{\mathrm{app}} \cdot \boldsymbol{\epsilon}^{\mathrm{p}}(\boldsymbol{\phi}(\boldsymbol{x})), & \boldsymbol{x} \in \text{material 1} \\[2mm] \boldsymbol{\sigma}_{\mathrm{app}} \cdot [\boldsymbol{\epsilon}^{\mathrm{p}}(\boldsymbol{\phi}^{\dagger}(\boldsymbol{x})) + \boldsymbol{\epsilon}^{\mathrm{v}}(\boldsymbol{x})], & \boldsymbol{x} \in \text{material 2} \end{cases}
\tag{30}
$$

Here, three TDGL equations are used, i.e.,

$$
\dot{\phi}_\alpha = -m_0 \partial_{\phi_\alpha}(\psi_{\mathrm{ela}} + \psi_{\mathrm{lat}} - \psi_{\mathrm{ext}}) \quad \text{in material 1}
\tag{31}
$$

$$
\dot{\phi}_\alpha^{\dagger} = -m_0^{\dagger} \partial_{\phi_\alpha^{\dagger}}(\psi_{\mathrm{ela}} + \psi_{\mathrm{lat}} - \psi_{\mathrm{ext}}) \quad \text{in material 2}
\tag{32}
$$

$$
\dot{\epsilon}_{ab}^{\mathrm{v}} = -m_0^{\mathrm{v}} \partial_{\epsilon_{ab}^{\mathrm{v}}}(\psi_{\mathrm{ela}} - \psi_{\mathrm{ext}}) \quad \text{in material 2}
\tag{33}
$$

where $a, b = 1, 2, 3$. Again, the Ginzburg–Landau coefficients m_0, $m_0^{\dagger}$, and m_0^{v} are not necessarily the same but should all be positive.

3.3. Material 2 as a vacuum

As a special case of a heterogeneous bimaterial medium, we treat material 2 as a vacuum, in which case $\boldsymbol{C}^{[2]}(\boldsymbol{x}) = \boldsymbol{0}$. Then in material 2, $\Delta C_{mnpq}(\boldsymbol{x}) = -C_{mnpq}^{[1]}$ according to Eq. (15). It follows that

$$
M_{ijkl}(\boldsymbol{x}) = C_{ijmn}^{[1]}[C_{mnpq}^{[1]}]^{-1} C_{pqkl}^{[1]} - C_{ijkl}^{[1]} = \delta_{ip}\delta_{jq} C_{pqkl}^{[1]} - C_{ijkl}^{[1]} = C_{ijkl}^{[1]} - C_{ijkl}^{[1]} = 0
\tag{34}
$$

Then,

$$
\psi_{\mathrm{ela}}(\boldsymbol{x}) = \begin{cases} \psi_{\mathrm{ela}}^{\mathrm{eq}}(\boldsymbol{\phi}(\boldsymbol{x})), & \boldsymbol{x} \in \text{material 1} \\[2mm] 0, & \boldsymbol{x} \in \text{material 2} \end{cases}
\tag{35}
$$

and Eqs. (23)–(26) hold.

This formulation accounts for the long-range interaction between a dislocation and a vacuum phase and has been employed in PFDD to study dislocation evolution near a void [38] and in PFM to study crack propagation in single crystals [46] and polycrystals [47] as well as dislocation dynamics in thin films [48]. However, it does not account for the short-range interactions between the dislocation and vacuum. In actuality, when a dislocation intersects with a vacuum, such as a free surface or a void, it leaves a ledge on the surface. An example can be seen in many prior atomistic simulations, which show that when an edge dislocation bypasses a void via the shearing mechanism, it leaves two steps on the void surface, where it enters and where it leaves. This phenomenon occurs in FCC [11,49], BCC [10,50], and HCP [51] materials. To account for both the short-range and long-range interactions, we model the void as a crystalline material with the same lattice constant as the matrix but with exceedingly low elastic moduli and GSFEs, as will be outlined in Section 5.2. We refer to this shearable void as a "pseudo-void" and will study its interactions with a dislocation in Section 6.

4. PFDD simulations

4.1. Model parameters

In this work, matrices and crystalline precipitates are either FCC or BCC phases. Since we focus on a single slip plane in this paper, $n_{\mathrm{sp}} = n_{\mathrm{op}}$. In FCC metals, the preferred slip plane is {111}, in which there are three slip vectors, i.e., $n_{\mathrm{sp}} = 3$, each of which lies along a $\langle 110 \rangle$ direction with $b_\alpha = \sqrt{2}a_0/2$ [41]. Hence, γ_{gsf} is represented by a GSFE surface, and $l_{\mathrm{gsf}} = d_\alpha = \sqrt{3}a_0/3$. In BCC metals, there are three possible types of glide planes: {110}, {112} and {123} [31]. Here, we focus on the {110} slip plane, for which $l_{\mathrm{gsf}} = d_\alpha = \sqrt{2}a_0/2$. Since the dislocation
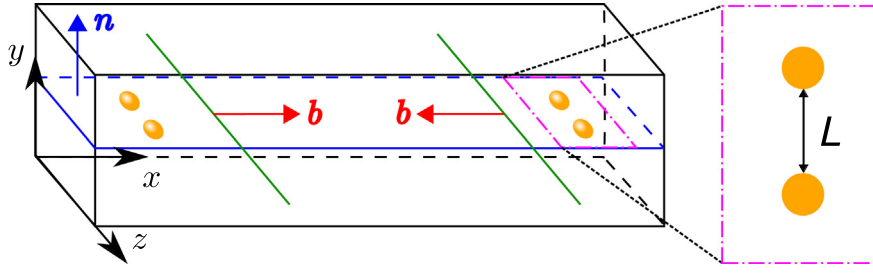
Fig. 1. Schematic of the simulation box set-up for an edge dislocation dipole interacting with two arrays of obstacles.

Table 1
Grid spacings along each direction in the FCC and BCC matrix materials. The values for a_0, the lattice parameter, are summarized in Table 2.

	h_x	h_y	h_z
FCC	$\frac{\sqrt{2}}{4}a_0$	$\frac{\sqrt{3}}{3}a_0$	$\frac{\sqrt{6}}{4}a_0$
BCC	$\frac{\sqrt{3}}{2}a_0$	$\frac{\sqrt{2}}{2}a_0$	$\frac{\sqrt{6}}{3}a_0$

is not dissociated, $n_{\text{sp}} = 1$ and γ_{gsf} is represented by a GSFE curve along the $\langle 111 \rangle$ direction. The only slip vector, with $b_\alpha = \sqrt{3}a_0/2$ [30], lies along the same direction.

4.2. Simulation set-up

As illustrated in Fig. 1, a dislocation dipole consisting of two edge dislocations with opposite Burgers vectors is built into a 3D periodic simulation box, which has lattice orientations

$$(\boldsymbol{i}_x, \boldsymbol{i}_y, \boldsymbol{i}_z) = \left(\frac{\sqrt{2}}{2}[\bar{1}10], \frac{\sqrt{3}}{3}[111], \frac{\sqrt{6}}{6}[11\bar{2}] \right) \tag{36}$$

in an FCC matrix, and

$$(\boldsymbol{i}_x, \boldsymbol{i}_y, \boldsymbol{i}_z) = \left(\frac{\sqrt{3}}{3}[111], \frac{\sqrt{2}}{2}[\bar{1}10], \frac{\sqrt{6}}{6}[\bar{1}\bar{1}2] \right) \tag{37}$$

in a BCC matrix. Let L_x, L_y, and L_z be the edge length of the simulation cell along the x, y, and z directions, respectively. Within each dipole, the two dislocation lines are along the z axis, lie on the mid-y plane, and are separated by $L_x/2$ along the x direction. Grid spacings along the three directions, h_x, h_y, and h_z, are summarized in Table 1. Along the x, y, and z directions, 256, 64, and 128 grid points are employed, respectively. To assess the model size effect, we doubled the grid point number along all three directions and found that the critical stresses varied by less than 2%.

Two arrays of spherical obstacles are placed on the mid-y plane and separated by $3L_x/4$ along the x direction. In each case, all obstacles are either unshearable voids, shearable voids (i.e., pseudo-voids), unshearable amorphous precipitates, or shearable, coherent crystalline precipitates. The crystallographic orientations of a shearable obstacle follow Eq. (36) or Eq. (37), depending on its lattice. Regardless of the obstacle type, each obstacle has a diameter of approximately 2.5 nm, and each array contains 1, 2, 4, 6, or 8 equally spaced obstacles, with the spacing L illustrated in Fig. 1.

4.3. Energy minimization and critical stresses

The elastic energy density ψ_{ela} is calculated by the fast Fourier transform method with the help of Green's functions. All Ginzburg–Landau coefficients are set to unity and the timestep size $\Delta t = 0.02$. In a heterogeneous medium, at each timestep, Eqs. (25)–(26) or Eqs. (31)–(33) are solved sequentially. Specifically, Eq. (25) or Eq. (31)

Table 2
Lattice parameters a_0 (in Å), elastic constants C_{11}, C_{12}, and C_{44} (in GPa), and isotropic shear modulus in Voigt form μ (in GPa) in Cu and Nb. Values of a_0 are from prior DFT calculations in Cu [52] and Nb [31], while those of elastic constants are from experiments [53].

	a_0	C_{11}	C_{12}	C_{44}	μ
Cu	3.634	169	122	75.3	54.58
Nb	3.324	245	132	28.4	39.64

is first iterated for all ϕ_α in material 1, resulting in new energy densities. Then Eq. (32) is iterated for all $\phi_\alpha^\dagger$ in material 2, again updating the energy densities. Finally, Eq. (26) or Eq. (33) is iterated for all ϵ_{ab}^v in material 2.

In the simulations that follow, two critical stresses will be determined. One is the Peierls stress, σ_P, the critical local stress required for a dislocation to move on its plane without any obstacles. The procedure used in PFDD to calculate it can be found in Ref. [40]. The other stress is σ_c, the critical stress for the dislocation to bypass the obstacle array. The minimum applied stress subject to which the critical event happens is recorded as σ_0, and the critical stress (either σ_P or σ_c) is $\sigma_0 - \Delta\sigma_0/2$, where $\Delta\sigma_0$ is the incremental resolved shear stress. Here, $\Delta\sigma_0 = 10^{-4}\mu$, where $\mu = (3C_{44} + C_{11} - C_{12})/5$ is the isotropic shear modulus in Voigt form for the matrix. Values of μ are summarized in Table 2. In particular, the xy and yx components of the stress tensor $\boldsymbol{\sigma}_{\text{app}}$ are non-zero. For each resolved shear stress, iterations are terminated when the Euclidean norm of the difference in global vector of each order parameter and each virtual strain between successive iterations is smaller than 10^{-5}. Static dislocation core structures and Peierls stresses in Cu and Nb in the absence of any obstacles are presented in Appendix B, while the critical stresses for dislocation/obstacle interactions will be discussed in details in Section 6.

4.4. Disregistry

To identify the dislocation core structures, the continuum disregistry field $\boldsymbol{\xi}$ is calculated as an instantiation of the discrete atomic displacements [41], i.e.,

$$\xi_\eta = \sum_{\alpha=1}^{n_{\text{sp}}} \phi_\alpha \boldsymbol{b}_\alpha \cdot \boldsymbol{s}_\eta \tag{38}$$

where η is the direction of ξ_η. In an FCC metal, η can be 1 or 2, representing respectively, the directions along and normal to the perfect dislocation Burgers vector. In other words, ξ_1 and ξ_2, respectively, are disregistry fields for the $\langle 110 \rangle$ and $\langle 112 \rangle$ directions. In a BCC metal, η can only be 1 and ξ_1 is the disregistry field for the $\langle 111 \rangle$ direction.

5. Material parameters

5.1. Matrices

Two matrices, Cu and Nb, are considered in this work. For each matrix, the material parameters needed for PFDD include lattice parameter a_0, elastic tensor $\boldsymbol{C}$, and GSFE surface/curve. Lattice parameters and GSFEs are based on prior density functional theory (DFT) calculations in Cu [52] and Nb [31]. Elastic constants are from prior experiments [53]. These relevant input are summarized in Table 2.

5.2. Pseudo-voids

As discussed in Section 3.3, in prior PF dislocation models involving vacuums (e.g., voids, cracks, and free surfaces), the short-range dislocation/vacuum interactions were not considered. As a result, the vacuum was unshearable by dislocations. In this work, the interest lies in representing the effect voids have on dislocation glide and so the void needs to be shearable by the dislocation. To this purpose, we treat a void as a second crystalline
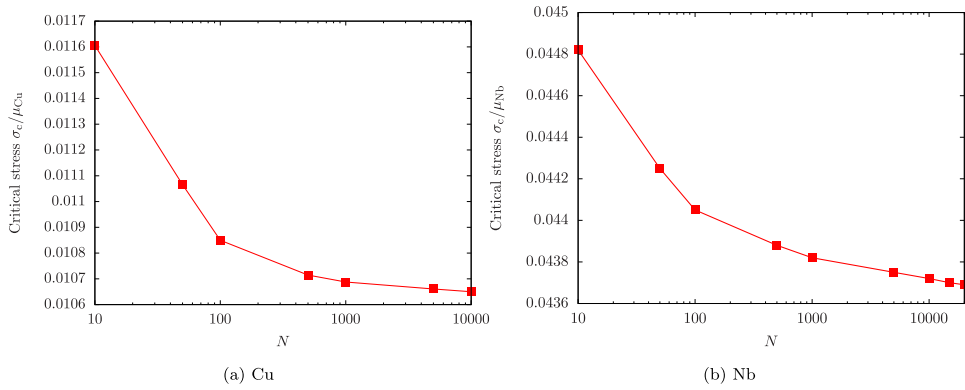
Fig. 2. (a) Critical bypass stress for a pseudo-void in (a) Cu and (b) Nb as a function of N for void spacing $L = 6h_z$.

phase with a set of non-zero order parameters and exceedingly low moduli and GSFEs. Since an actual void has zero ψ_{ela} and ψ_{lat}, the shearable void can be considered a "pseudo-void".

We first ensure that the critical stresses calculated are affected negligibly by the choice of pseudo-void properties. For the sake of simplicity, we reduce all elastic constants and lattice energies uniformly, via

$$C_{ijkl}^{\text{pv}} = C_{ijkl}^{\text{matrix}}/N, \quad \gamma_{\text{gsf}}^{\text{pv}} = \gamma_{\text{gsf}}^{\text{matrix}}/N \tag{39}$$

where N is a positive integer. For this test, we consider the case with the greatest void volume fraction studied here, where the void spacing $L = 6h_z$. Fig. 2 shows the change in the critical stress as N increases, or equivalently as the energy densities in the void decrease. It is found that the critical stress for a dislocation to bypass eight pseudo-voids decreases with N, suggesting that obstacles with smaller elastic constants and lower GSFEs are weaker barriers to dislocation glide. We find that when $N = 10\,000$ and $20\,000$, respectively, the critical stress converges in Cu and Nb. These two values of N, which depend on the matrix material but not on the pseudo-void spacing, will be used in subsequent PFDD simulations.

5.3. Precipitates

The precipitates considered in this paper are $\text{Cu}_{1-x}\text{Nb}_x$ alloys, where x varies from 0.1 to 0.9. Depending on the composition, the precipitate in its stable form is either an amorphous or a crystalline solid. Due to the high computational cost of DFT, we resort to atomistic simulations, using LAMMPS [54], to determine the material parameters for precipitates. In Section 5.3.2, we will identify the most stable phase of $\text{Cu}_{1-x}\text{Nb}_x$ and calculate the lattice parameters of the crystalline phases. Then in Sections 5.3.3 and 5.3.4, respectively, we will calculate the elastic constants of all precipitates and GSFEs of the crystalline precipitates.

5.3.1. Interatomic potentials

The embedded-atom method (EAM) potential developed by Zhang et al. [55] is used for the Cu–Nb system. The potential was recently used to study the confined layer slip in Cu/Nb nanolaminates [56]. In prior works, it was demonstrated that this potential can reproduce lattice parameters and elastic constants in Cu and Nb in agreement with DFT [57,58]. Here, using the EAM potential we also calculate the relaxed GSFE curves in Cu and Nb and compare them with prior DFT calculated curves in Refs. [31,52]. The method to calculate the relaxed GSFE curves follows Ref. [59] on the {111} plane in Cu and Ref. [60] on the {110} plane in Nb. Results, shown in Fig. 3, indicate that EAM potential is reasonably accurate in predicting GSFEs in the two metals. In Nb, the {110}⟨111⟩ curve has one maximum, according to DFT [31], while the EAM potential slightly overestimates the peak energy and produces a shallow local minimum. Similar discrepancy was found between the two {112}⟨111⟩ GSFE curves [58].
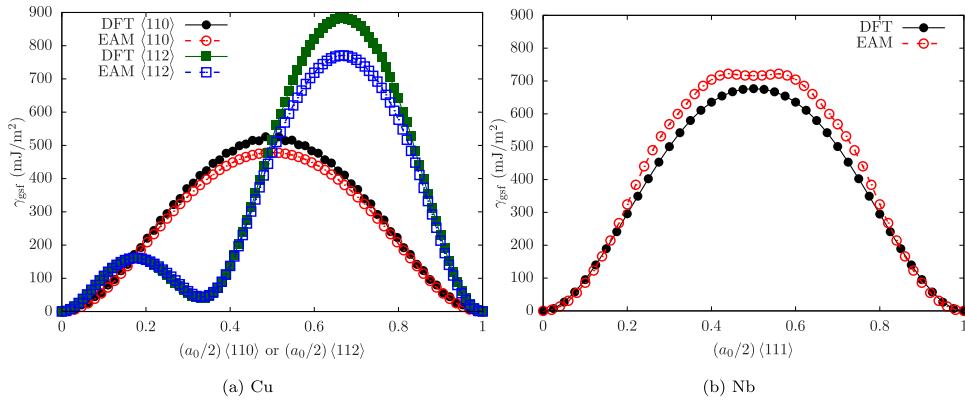
Fig. 3. Relaxed GSFE curves (a) for two crystallographic directions on the {111} plane in Cu and (b) for the {110} plane in Nb. DFT results are taken from Ref. [52] for Cu and Ref. [31] for Nb.
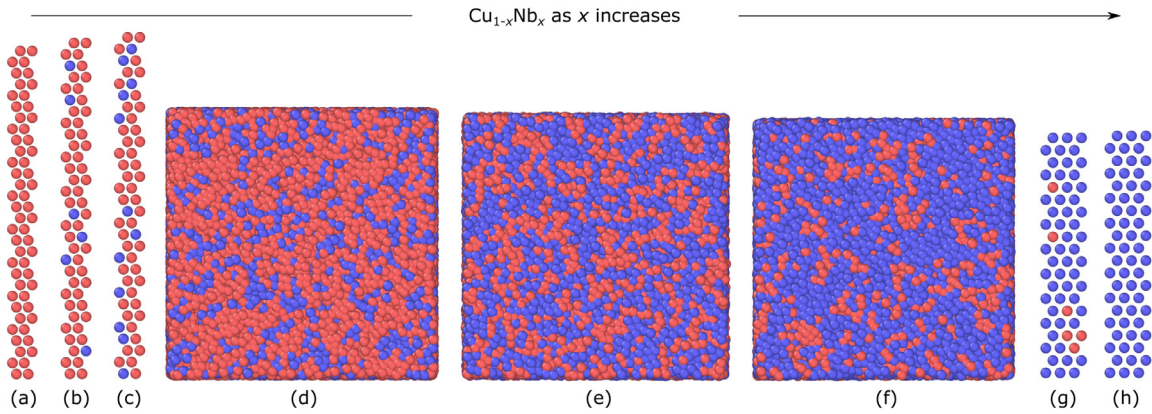

Fig. 4. Atomistic structures of the eight materials listed in Table 3: (a) FCC Cu, (b) FCC $Cu_{0.9}Nb_{0.1}$, (c) FCC $Cu_{0.8}Nb_{0.2}$, (d) amorphous $Cu_{0.7}Nb_{0.3}$, (e) amorphous $Cu_{0.5}Nb_{0.5}$, (f) amorphous $Cu_{0.3}Nb_{0.7}$, (g) BCC $Cu_{0.1}Nb_{0.9}$, and (h) BCC Nb. Visualization is enabled by OVITO [65]. Red and blue atoms are Cu and Nb, respectively. For better display, the simulation cells in (d), (e), and (f) are reduced in size by 50% in all three directions, with respect to the remaining five structures. (For interpretation of the references to color in this figure legend, the reader is referred to the web version of this article.)

5.3.2. Identification of the most stable phase of $Cu_{1-x}Nb_x$

Eleven chemical compositions are considered, as x increases from 0 to 1, in increments of 0.1. For a given x, where $x \neq 0$ and $\neq 1$, special quasi-random structures (SQS) [61] in FCC and BCC phases are built using ATAT [62]. Each SQS contains 60 atoms. When $x = 0$ or 1, atomic structures of pure metals, including FCC Cu, FCC Nb, BCC Cu, and BCC Nb, each of which contains 60 atoms, are built. For each crystalline structure, we calculate the lattice parameter a_0 via the volume-energy method [63,64], with the cohesive energy as a byproduct. Selected atomistic crystalline structures are presented in Fig. 4(a,b,c,g,h).

Compared with crystalline structures, constructing amorphous structures is less straightforward. For each composition, six steps are taken. First, Cu and Nb atoms at specified compositions are randomly assigned to a simulation cell sized approximately 10 nm × 10 nm × 10 nm. Second, the structure is energy minimized via the conjugate gradient method, while the simulation cell size is allowed to change to zero all three normal stresses. In each energy minimized structure, if two atoms are closer to each other than 1.1 Å, one of them is deleted. Each structure contains 42 000 ∼ 70 000 atoms, depending on the composition. Third, under an NPT ensemble, the structure is then heated at a rate of 3.5×10^{14} K/s to 3500 K, well above the liquidus line on the phase diagram specified by the EAM potential [55]. Fourth, the temperature is kept at 3500 K for 10 ps under an NPT ensemble. Fifth, the structure is cooled down from 3500 K to 1 K at a rate of -10^{12} K/s. Last, energy minimization is conducted using the conjugate gradient method, while all normal stresses are again zeroed. Selected atomistic
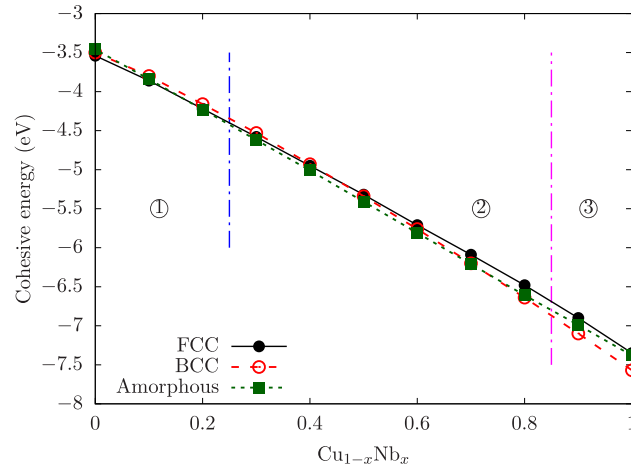
Fig. 5. EAM-based cohesive energies for $Cu_{1-x}Nb_x$ as x varies from 0 to 1, in increments of 0.1. In regions 1, 2, and 3, FCC, amorphous, and BCC phases, respectively, have the lowest cohesive energy.
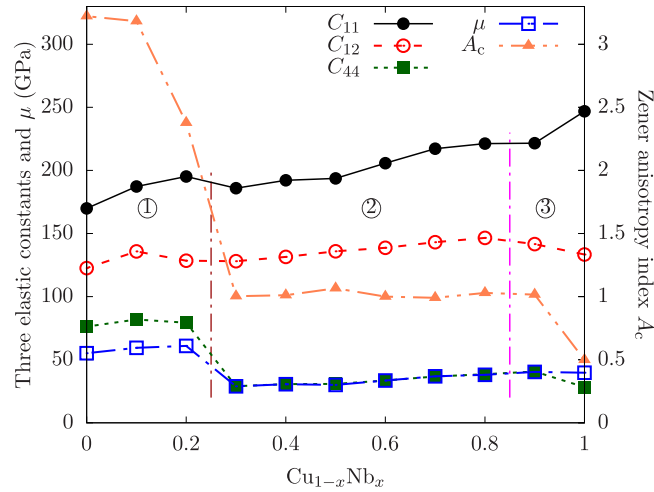

Fig. 6. EAM-based elastic constants C_{11}, C_{12}, and C_{44} of $Cu_{1-x}Nb_x$, as x varies from 0 to 1. The Voigt isotropic shear moduli μ and Zener anisotropy indices A_c are also presented. In regions 1, 2, and 3, FCC, amorphous, and BCC, respectively, are the most stable phases.

amorphous structures are presented in Fig. 4(d,e,f). The cohesive energy is then calculated. For each composition, five random samples are considered and the resultant cohesive energies differ within 1%. For selected compositions, a lower cooling rate of -10^{11} K/s is tried and the results differ within 0.5%. In all dynamic simulations, a timestep size of 1 fs is used.

Fig. 5 shows the cohesive energies of $Cu_{1-x}Nb_x$, for x varying from 0 to 1 in increments of 0.1. For each composition, cohesive energies based on an FCC, a BCC, and an amorphous phase are compared. Three regions are identified. Region 1 spans $x \leq 0.2$, wherein the FCC phase has the lowest cohesive energy. Region 2 covers $0.3 \leq x \leq 0.8$, and corresponds to the amorphous phase with the lowest cohesive energy. Finally, region 3 spans $x \geq 0.9$, where the BCC phase has the lowest cohesive energy. In other words, the $Cu_{1-x}Nb_x$ alloy is amorphous in the range of 15–75 at.% Cu, which agrees with the experimental result of 35–74 at.% Cu relatively well [66].

5.3.3. Elastic constants

The elastic constants C_{11}, C_{12}, and C_{44} of $Cu_{1-x}Nb_x$ in their stable phases, for x varying from 0 to 1, are calculated via the stress–strain method [63,64] and presented in Fig. 6. According to the Zener anisotropy index

Table 3

EAM-based lattice parameters a_0 (in Å) and elastic constants C_{11}, C_{12}, and C_{44} (in GPa) of the six $Cu_{1-x}Nb_x$ precipitates studied in this work. Isotropic shear modulus in Voigt form μ (in GPa) and Zener anisotropy index A_c are also presented. EAM-based values for Cu and Nb, which are not used for input in the present PFDD simulations, are included here to show that they are close to the DFT-based values (Table 2). Atomistic structures used in all calculations here are presented in Fig. 4.

	Phase	a_0	C_{11}	C_{12}	C_{44}	μ	A_c
Cu	FCC	3.613	169.9	122.6	76.2	55.18	3.22
$Cu_{0.9}Nb_{0.1}$	FCC	3.699	187.25	135.8	81.88	59.42	3.18
$Cu_{0.8}Nb_{0.2}$	FCC	3.759	195.16	128.44	79.32	60.94	2.38
$Cu_{0.7}Nb_{0.3}$	Amorphous		185.9	128.1	29	28.96	1
$Cu_{0.5}Nb_{0.5}$	Amorphous		193.7	135.9	30.8	30.04	1.07
$Cu_{0.3}Nb_{0.7}$	Amorphous		217.2	143.1	36.7	36.84	0.99
$Cu_{0.1}Nb_{0.9}$	BCC	3.274	221.58	141.63	40.63	40.37	1.02
Nb	BCC	3.3	246.9	133.4	28.3	39.68	0.5
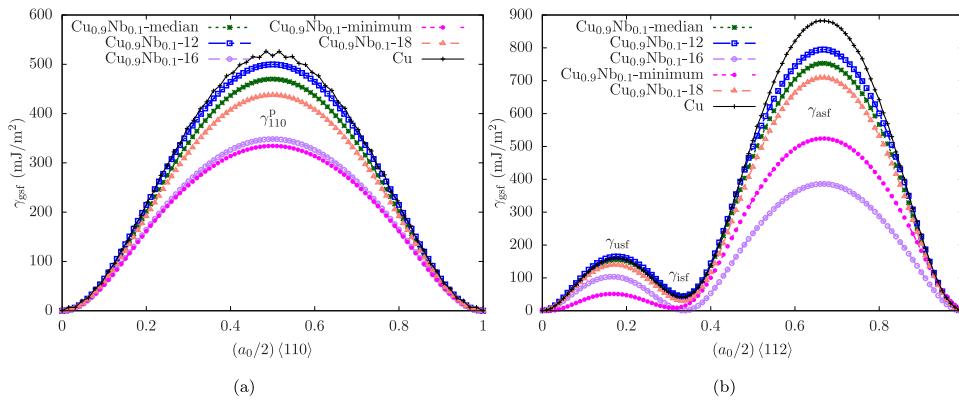
Fig. 7. Relaxed GSFE curves in the (a) $\langle 110 \rangle$ direction and (b) $\langle 112 \rangle$ direction on $\{111\}$ plane in FCC $Cu_{0.9}Nb_{0.1}$. DFT data for Cu from Ref. [52] are presented for reference.

$A_c = 2C_{44}/(C_{11} - C_{12})$, Cu, Nb, and two FCC precipitates, $Cu_{0.9}Nb_{0.1}$ and $Cu_{0.8}Nb_{0.2}$, are highly elastically anisotropic, while all other precipitates, whether BCC or amorphous, are nearly elastically isotropic. The latter results are expected because the amorphous materials are elastically isotropic.

In subsequent PFDD simulations, we will consider the following four precipitate compositions: (i) FCC $Cu_{0.9}Nb_{0.1}$, (ii) FCC $Cu_{0.8}Nb_{0.2}$, (iii) amorphous $Cu_{0.7}Nb_{0.3}$, (iv) amorphous $Cu_{0.5}Nb_{0.5}$, in a Cu matrix. In a Nb matrix, we will presume the precipitates are one of these three compositions: (iv) amorphous $Cu_{0.5}Nb_{0.5}$, (v) amorphous $Cu_{0.3}Nb_{0.7}$, and (vi) BCC $Cu_{0.1}Nb_{0.9}$. The values of a_0, C_{11}, C_{12}, and C_{44} of the six distinct compositions are summarized in Table 3. Comparison of the moduli between precipitates and matrices reveals an elastic moduli mismatch, an effect that is directly taken into account in the present PFDD formulation. Comparison of the lattice parameters between crystalline precipitates and matrices reveals that the interfaces are coherent or semi-coherent, justifying our choices of neglecting the coherent strain made in Section 3.2.

5.3.4. GSFEs

As mentioned in Section 4.1, γ_{gsf} is represented by a GSFE surface and a GSFE curve, respectively, in FCC and BCC crystals. For an alloy, the fraction of solutes in adjacent to different, parallel crystallographic planes can vary, deviating from the atomic volume fraction. For heavily alloyed metals, like MPEAs, the variation can be significant [67–69]. For the dilute alloys here, the variation is smaller, yet we still repeat the GSFE calculations for all parallel planes within the same SQS.

In FCC alloys, i.e., $Cu_{0.9}Nb_{0.1}$ and $Cu_{0.8}Nb_{0.2}$, the SQS for each precipitate composition contains 30 $\{111\}$ planes (Fig. 4(b,c)), for which we calculate 30 GSFE surfaces. Selected GSFE curves along $\langle 110 \rangle$ or $\langle 112 \rangle$ direction are
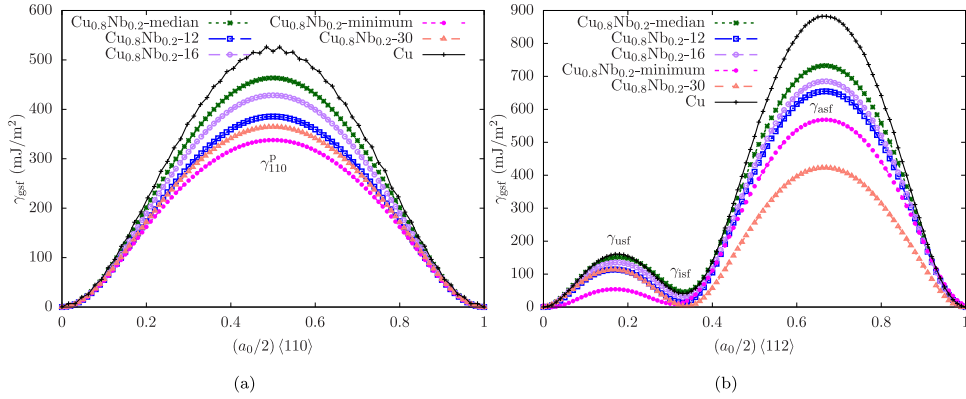
Fig. 8. Relaxed GSFE curves in the (a) $\langle 110 \rangle$ direction and (b) $\langle 112 \rangle$ direction on $\{111\}$ plane in FCC $Cu_{0.8}Nb_{0.2}$. DFT data for Cu from Ref. [52] are presented for reference.

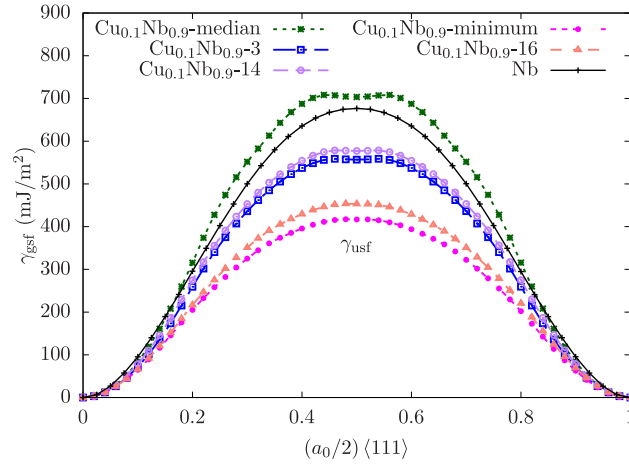**Fig. 9.** Relaxed GSFE curves along the $\langle 111 \rangle$ direction on the $\{110\}$ plane in BCC $Cu_{0.1}Nb_{0.9}$. DFT data for Nb from Ref. [31] are given for reference.

presented in Figs. 7 and 8. In each alloy, the GSFEs vary significantly and most of them are lower than those in Cu. The median and minimum values of the peak GSFE value along the $\langle 110 \rangle$ curve, γ_{110}^{p}, are, respectively, 470.04 mJ/m^2 and 334.42 mJ/m^2 in $Cu_{0.9}Nb_{0.1}$, which are about 9% and 36% lower than that in Cu, 519.05 mJ/m^2. The minimum γ_{110}^{p} in $Cu_{0.8}Nb_{0.2}$ is even lower, 330.89 mJ/m^2. Similar trends are found for local minima and maxima on the GSFE curve along the $\langle 112 \rangle$ direction, including unstable SFE γ_{usf}, intrinsic SFE γ_{isf}, and aligned SFE γ_{asf}. These SFEs, defined in Ref. [52], are summarized in Table 4. Despite the wide variation in the GSFEs among different planes and alloys, the shape of the GSFE surfaces remains largely unchanged, similar to a prior finding in an FCC MPEA [67].

To analyze the effects of the GSFE on dislocation/precipitate interactions, the median or minimum GSFE surfaces in the two alloys will be used in Section 6.2.1. Values of the four GSFE surfaces roughly follow

$$Cu_{0.9}Nb_{0.1}\text{-median} > Cu_{0.8}Nb_{0.2}\text{-median} > Cu_{0.9}Nb_{0.1}\text{-minimum} > Cu_{0.8}Nb_{0.2}\text{-minimum} \qquad (40)$$

In the BCC alloy, i.e., $Cu_{0.1}Nb_{0.9}$, the SQS contains 20 $\{110\}$ planes (Fig. 4(g)), for which we calculate 20 GSFE curves along the $\langle 111 \rangle$ direction. Selected GSFE curves are presented in Fig. 9. The median and minimum γ_{usf} values are 703.46 mJ/m^2 and 416.96 mJ/m^2, respectively, which are 4% higher and 38% lower than that in Nb, 676.78 mJ/m^2. Despite the large variation, the shape of the GSFE curves among different planes are similar, in line

Table 4

Peak GSFE value along the $\langle 110 \rangle$ curve $\gamma_{110}^{\mathrm{p}}$, unstable SFE γ_{usf}, intrinsic SFE γ_{isf}, and aligned SFE γ_{asf} of the three $\mathrm{Cu}_{1-x}\mathrm{Nb}_x$ crystalline precipitates studied in this work. Values of Cu [52] and Nb [31] based on prior DFT calculations are presented for reference. All are in units of mJ/m^2.

	Phase	$\gamma_{110}^{\mathrm{p}}$	γ_{usf}	γ_{isf}	γ_{asf}
Cu	FCC	519.05	160.52	41.83	891.28
$\mathrm{Cu}_{0.9}\mathrm{Nb}_{0.1}$-median	FCC	470.04	155.19	40.67	752.91
$\mathrm{Cu}_{0.9}\mathrm{Nb}_{0.1}$-minimum	FCC	334.42	51.41	8.45	524.2
$\mathrm{Cu}_{0.8}\mathrm{Nb}_{0.2}$-median	FCC	463.52	151.18	38.17	732.62
$\mathrm{Cu}_{0.8}\mathrm{Nb}_{0.2}$-minimum	FCC	330.89	50.05	6.37	518.5
$\mathrm{Cu}_{0.1}\mathrm{Nb}_{0.9}$-median	BCC		703.46		
$\mathrm{Cu}_{0.1}\mathrm{Nb}_{0.9}$-minimum	BCC		416.96		
Nb	BCC		676.78		
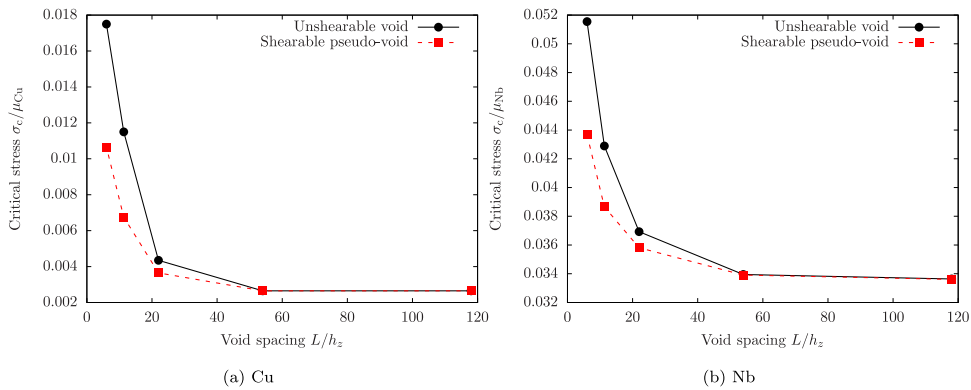
Fig. 10. Comparison between the critical bypass stresses for pseudo-voids and unshearable voids in (a) Cu and (b) Nb.

with a prior finding in two BCC MPEAs [68]. The artificial local minimum at γ_{usf} seen in pure Nb diminishes or even disappears in some of the GSFE curves in $\mathrm{Cu}_{0.1}\mathrm{Nb}_{0.9}$.

6. PFDD results

6.1. Unshearable vs. pseudo-voids

When voids are present in the matrix, they are expected to act as obstacles to dislocation motion. The resistance they impose depends on the mechanism by which the dislocation uses to circumvent them. Fig. 10(a) compares the calculated critical stresses for the dislocation to bypass a row of pseudo-voids or unshearable voids in Cu for a range of void spacings L. For $L \geq 54h_z$, the differences between the critical stress for the pseudo-voids and unshearable voids diminish. These critical stresses are no longer dependent on L, as well, and reduce to $0.00265\mu_{\mathrm{Cu}}$. They draw close in value to the Peierls stress σ_{P}, $0.00255\mu_{\mathrm{Cu}}$. Voids are such weak obstacles to dislocation motion that once their spacing becomes much larger than the dislocation core width (for Cu, 2.31 nm) that they become ineffective at hindering the glide of a dislocation.

As L reduces to $22h_z$ and below, the effect of the pseudo-void becomes more pronounced. In this fine range of spacing, the critical bypass stress for the pseudo-void is lower than that for an unshearable one. At a given fine L, σ_{c} for pseudo-voids are about 39% lower than those for unshearable voids. For either the pseudo-void or unshearable void, as L decreases further, σ_{c} increases, a trend that agrees with atomistic simulations [51,70] and elasticity theory [71,72]. Also, when the spacing is fine, voids become formidable obstacles. In Cu, for the finest L of $6h_z$, which is smaller than the stress-free stacking fault width, σ_{c} for pseudo-voids have increased by 317% compared with the Peierls stress.

Fig. 10(b) presents σ_{c} for the edge dislocation in Nb to bypass a row of pseudo-voids or unshearable voids for the same range of void spacings L. For the two largest L, $54h_z$ and $118h_z$, σ_{c} are almost the same, $\approx 0.034\mu_{\mathrm{Nb}}$, for
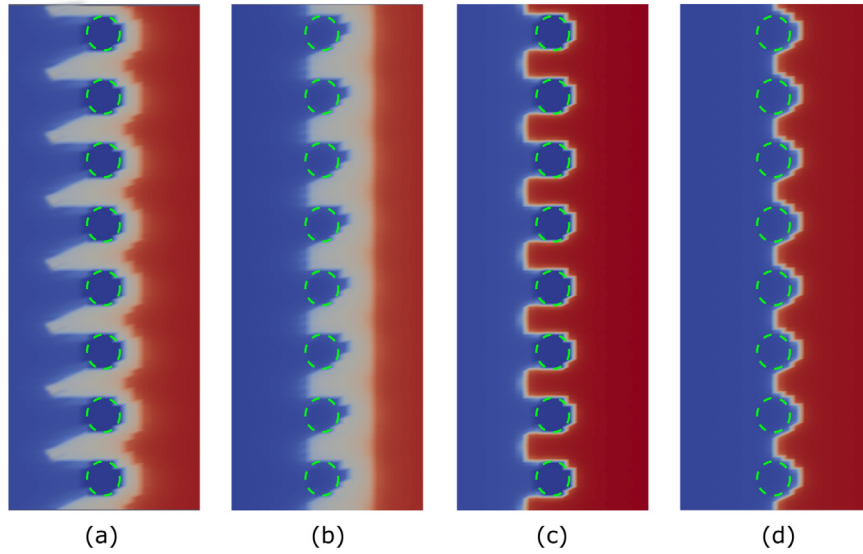
Fig. 11. Snapshots of critical configurations for an edge dislocation bypassing eight (a) unshearable voids in Cu, (b) pseudo-voids in Cu, (c) unshearable voids in Nb, and (d) pseudo-voids in Nb. The void spacing $L = 6h_z$. All snapshots are taken at applied stresses that are slightly lower than the corresponding critical stresses and are colored by the disregistry ξ_1 (Eq. (38)), where blue and red correspond to $\xi_1 = 0$ and b, respectively. Voids are denoted by dashed green circles. (For interpretation of the references to color in this figure legend, the reader is referred to the web version of this article.)

pseudo-voids and unshearable voids, and are slightly higher than the Peierls stress σ_P, $0.03355\mu_{Nb}$. As L decreases below $54h_z$, values of σ_c as well as differences between the pseudo-voids and unshearable voids increase. When $L = 22h_z$, σ_c for pseudo-voids is about 3% lower than that for unshearable voids; when $L = 6h_z$, the reduction is even greater, 15%. Compared with σ_P, at $L = 6h_z$, σ_c for pseudo-voids is 30% higher.

To further compare unshearable voids with the shearable ones, Fig. 11 shows the critical configuration of the dislocation as it attempts to bypass an array of closely spaced voids $L = 6h_z$, the finest spacing studied here. Without voids, the edge dislocation in both Cu and Nb remains straight as it glides since lengthening the dislocation would incur an increase in the system energy. With voids, however, the dislocation needs to balance between either bowing out between them, thereby increasing its length, or cutting through them, largely maintaining its length. In the case of unshearable voids, the critical configuration involves the dislocations extruding between voids. In contrast, in the case of pseudo-voids, the dislocation bows out to a lesser extent between the voids, before cutting them.

6.2. Crystalline precipitates

As summarized in Table 3, we consider three crystalline precipitates in this work: FCC $Cu_{0.9}Nb_{0.1}$, FCC $Cu_{0.8}Nb_{0.2}$, and BCC $Cu_{0.1}Nb_{0.9}$. The first two are in a Cu matrix while the last one is in a Nb matrix.

6.2.1. Crystalline precipitates in a Cu matrix

Here, we consider two crystalline precipitates in a Cu matrix: one composition is FCC $Cu_{0.9}Nb_{0.1}$ and the other FCC $Cu_{0.8}Nb_{0.2}$. As shown in Table 4, the GSFEs within these precipitates are lower than that of the Cu matrix. The lower the lattice energy, the easier it is for the partial dislocations to glide in the precipitate than that in Cu. To study representative examples, the simulations are carried out with precipitates with a median-level GSFE surface and those with a minimum-level GSFE surface, respectively. Compared to Cu, their effective isotropic shear modulus is higher (Table 3), which would cause the dislocation to resist transmitting through them.

Fig. 12 presents snapshots at different moments as an edge dislocation bypasses an array of $Cu_{0.8}Nb_{0.2}$ precipitates when the applied stress is slightly higher than the critical one, σ_c. In this case the spacing between adjacent precipitates (2.51 nm) is close to that of the intrinsic stacking fault width (2.31 nm). We observe that the portions of the leading partial dislocation that directly impinge on the precipitates are at first held back by the precipitates and
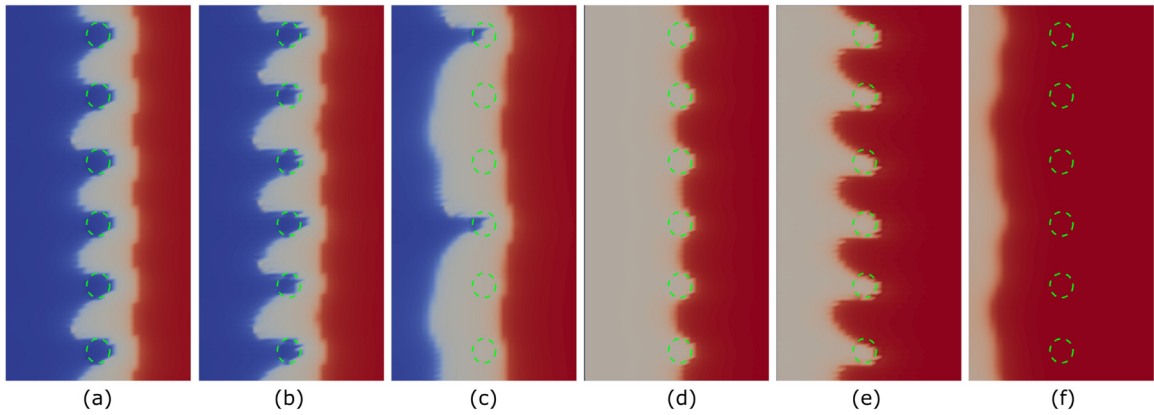
Fig. 12. Snapshots of selected configurations for an edge dislocation bypassing six FCC $Cu_{0.8}Nb_{0.2}$ precipitates with the median GSFE surface in a Cu matrix. The precipitate spacing $L = 11.3h_z$. The applied stress is constant and is slightly higher than the critical stress, $0.00795\mu_{Cu}$. All snapshots are colored in the same way as Fig. 11.
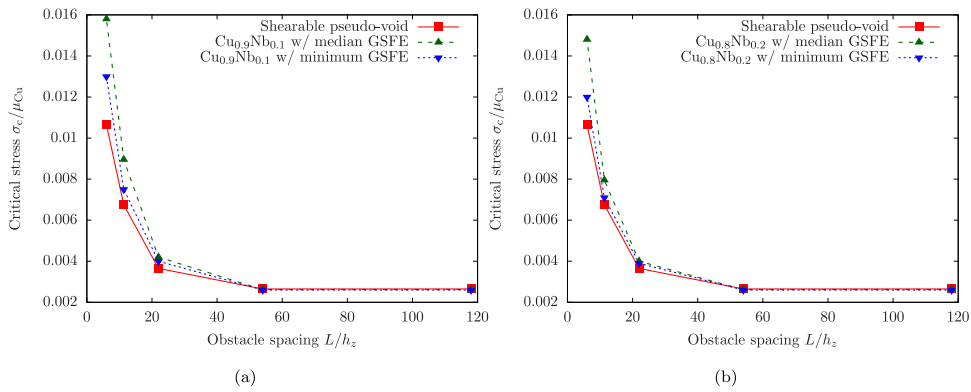

Fig. 13. In a Cu matrix, critical dislocation bypass stress as a function of the obstacle spacing L in the cases of (a) FCC $Cu_{0.9}Nb_{0.1}$ and (b) FCC $Cu_{0.8}Nb_{0.2}$ precipitates with the median or minimum GSFE surface. Results for pseudo-voids are presented as references.

the remaining parts extrude between them, as shown in Fig. 12(a,b). Next, the leading partial transmits through a pair of precipitates while being held back every third one in the array (Fig. 12(c)). Once the transmission is completed, the partial continues to glide, bowing out between every third precipitate. During this stage, the trailing partial remains more or less straight and thus the extruding dislocation causes the stacking fault to expand. Eventually, the leading partial transmits through the other precipitates and glides away, while the trailing partial approaches and impinges on the precipitate array in Fig. 12(d). It bows out between every precipitate (Fig. 12(e)) and eventually transmits through the latter. It follows that both the leading and trailing partial dislocations are able to continue gliding (Fig. 12(f)). Throughout this sequence, the critical stress is determined by the stress required for the leading partial to transmit through the first set of precipitates (between Fig. 12(b) and (c)).

For all precipitate spacings and compositions, the dislocation cuts through the precipitates in the sequence shown in Fig. 12. If the applied stress is sufficiently high for the leading partial dislocation to shear the precipitates, it is also sufficient for the trailing partial to shear them. It is interesting to note that the sequence of events for precipitates is different from that of the same dislocation meeting an array of pseudo-voids with the same L. First, the leading partial bows out further between the precipitates before transmitting through them. Second, the leading partial does not shear all precipitates at once, as it does in the case of the pseudo-void array. Both are consequences of the greater resistance to shear posed by the precipitates than the voids.

Fig. 13 compares the calculated σ_c for an edge dislocation to bypass an array of crystalline precipitates with their median and minimum GSFE surfaces for a broad range of L from $6h_z$ to $118h_z$. For large spacings, $L \geq 54h_z$, σ_c is
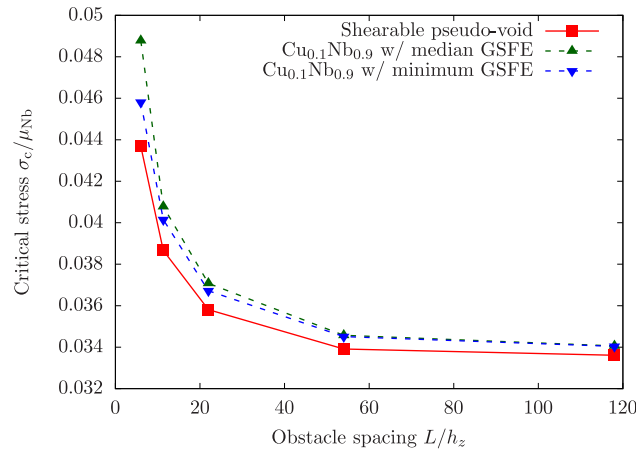
Fig. 14. In a Nb matrix, critical dislocation bypass stress as a function of the obstacle spacing L in the cases of pseudo-voids, BCC $Cu_{0.1}Nb_{0.9}$ precipitates with the median GSFE curve, and BCC $Cu_{0.1}Nb_{0.9}$ precipitates with the minimum GSFE curve.

nearly the same for both precipitate compositions: $Cu_{0.9}Nb_{0.1}$ and $Cu_{0.8}Nb_{0.2}$. These widely spaced obstacles pose little resistance against dislocation glide and differences in their elastic constants and GSFE due to composition have a negligible influence. For precipitates that are more finely spaced, $L = 22h_z$, the differences in precipitate GSFE and moduli emerge. Since these two alloys have similar isotropic shear modulus (Table 3), the differences in σ_c reflect those in their GSFE surfaces. Comparing Fig. 13(a) and (b) shows that σ_c increases with higher γ_{usf} in the precipitates. The influence of GSFE on σ_c increase as the spacing further decreases. When $L = 6h_z$, the highest value of $0.0158\mu_{Cu}$ is for the median GSFE in $Cu_{0.9}Nb_{0.1}$ while the lowest of $0.012\mu_{Cu}$ for the minimum GSFE in $Cu_{0.8}Nb_{0.2}$.

The critical stresses for bypassing pseudo-voids of the same size and spacing are superimposed in Fig. 13 for reference. Precipitates have non-negligible lattice energy and stiffness and are expected to be more formidable obstacles. Cu matrix that contains crystalline precipitates is strengthened, more so than that contains pseudo-voids. For example, when $L = 6h_z$, the critical stress for the weakest crystalline precipitate, i.e., $Cu_{0.8}Nb_{0.2}$ with the minimum GSFE surface, is about 13% and 371% higher than the critical stress for the pseudo-voids and the Peierls stress, respectively.

6.2.2. Crystalline precipitates in a Nb matrix

In this section, we consider one type of precipitate, $Cu_{0.1}Nb_{0.9}$, in a Nb matrix. We consider the precipitates having either a median-level or minimum-level GSFE curve. As shown in Fig. 9, the median GSFE in $Cu_{0.1}Nb_{0.9}$ is higher than the GSFE of Nb, while the minimum GSFE in $Cu_{0.1}Nb_{0.9}$ is lower. In addition, the $Cu_{0.1}Nb_{0.9}$ precipitate is slightly stiffer than Nb (Table 3).

Fig. 14 shows the critical stress σ_c for an edge dislocation to bypass an array of $Cu_{0.1}Nb_{0.9}$ precipitates in a Nb matrix, while varying their spacing L from $6h_z$ to $118h_z$. It is shown that the Nb matrix is strengthened by crystalline precipitates more than shearable pseudo-voids for all L. For large spacings, $L > 22h_z$, the effects of variation in GSFE diminish and their σ_c are nearly equal. For finer spacings, $L \le 22h_z$, the effects of precipitate GSFE on σ_c are heightened and their differences in σ_c grow as L reduces. As before, we observe that σ_c increases with γ_{usf}. σ_c for the precipitate with the median GSFE is 2% higher than that for the minimum GSFE when $L = 11.3h_z$, but even higher (6%) for $L = 6h_z$. When $L = 6h_z$ and with the median GSFE, σ_c is about 12% and 45% higher than the critical stress for the pseudo-voids and the Peierls stress, respectively.

Fig. 15 shows selected snapshots during the passage of an edge dislocation by widely spaced BCC $Cu_{0.1}Nb_{0.9}$ precipitates under a constant applied stress slightly higher than σ_c. The precipitates have the median GSFE, and thus, both the GSFE and shear moduli of the precipitates are higher than those of Nb. When the dislocation glides to the array (Fig. 15(a)), the portions that directly meet the precipitate are first held back at the precipitate, while the segments in between them bow out (Fig. 15(b)). As the dislocation continues to bow further, the portions held back at the precipitates partially wrap around them, as shown in Fig. 15(c,d). At some critical point, the dislocation
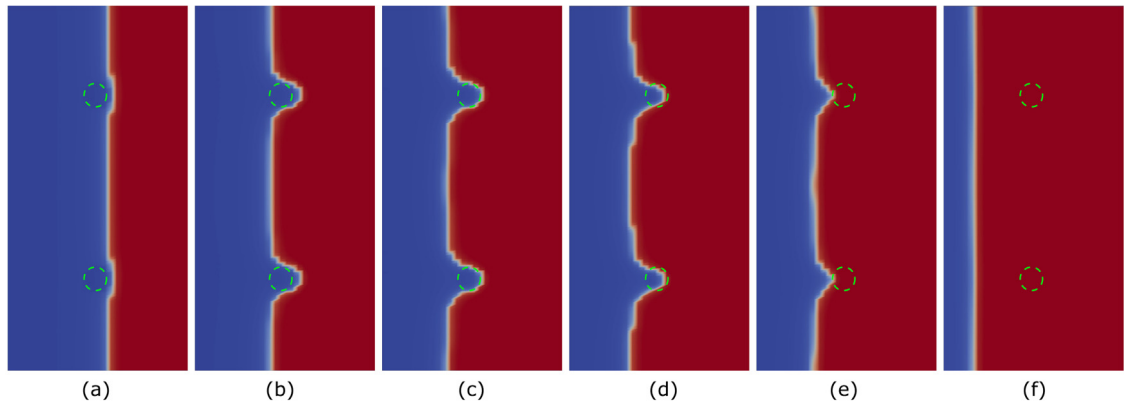
Fig. 15. Snapshots of selected configurations for an edge dislocation bypassing two BCC $Cu_{0.1}Nb_{0.9}$ precipitates with the median GSFE curve in a Nb matrix. The precipitate spacing $L = 54h_z$. The applied stress is constant and is slightly higher than the critical stress, $0.03555\mu_{Nb}$. All snapshots are colored in the same way as Fig. 11.
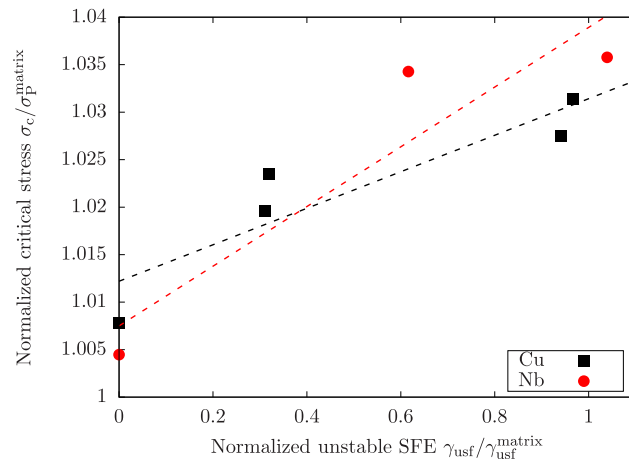

Fig. 16. Normalized critical stress for a dislocation to bypass a pseudo-void or a crystalline precipitate in Cu and Nb, with respect to the normalized unstable SFE of the obstacles. The obstacle spacing $L = 118h_z$, which closely represents an isolated obstacle. The dashed lines are linear fits: $\sigma_c/\sigma_P^{matrix} = 0.019\gamma_{usf}/\gamma_{usf}^{matrix} + 1.012$ for Cu and $\sigma_c/\sigma_P^{matrix} = 0.031\gamma_{usf}/\gamma_{usf}^{matrix} + 1.007$ for Nb.

no longer bows further and transmits through the precipitates (Fig. 15(e)). Finally, it straightens and glides away (Fig. 15(f)).

To identify a general relationship between σ_c and obstacle properties, the normalized critical stresses for the dislocation to bypass a pseudo-void or crystalline precipitate in Cu or Nb are plotted with respect to the normalized unstable SFE of the obstacle in Fig. 16. As shown, the two normalized quantities scale positively with each other in both matrices, with similar linear fit coefficients.

6.3. Amorphous precipitates

As summarized in Table 3, we consider three amorphous precipitates in this work: $Cu_{0.7}Nb_{0.3}$, $Cu_{0.5}Nb_{0.5}$, and $Cu_{0.3}Nb_{0.7}$. The first two are in a Cu matrix while the last two are in a Nb matrix. The isotropic shear modulus of these amorphous precipitates (29–37 GPa) are much lower than that of Cu (55 GPa) and slightly lower than that of Nb (40 GPa). Unlike the shearable pseudo-voids and crystalline precipitates, dislocations cannot glide within the amorphous precipitates.
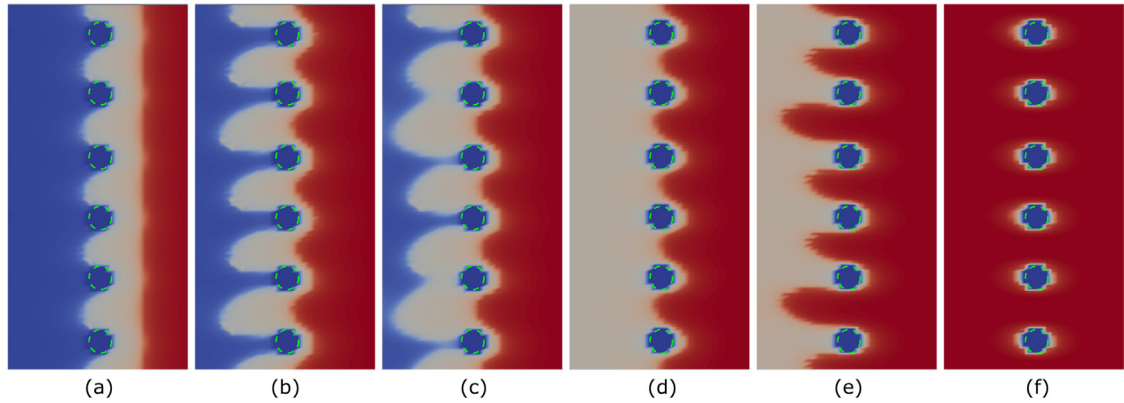
Fig. 17. Snapshots of selected configurations for an edge dislocation bypassing six amorphous $Cu_{0.5}Nb_{0.5}$ precipitates in a Cu matrix. The precipitate spacing $L = 11.3h_z$. The applied stress is constant and is slightly higher than the critical stress, $0.01105\mu_{Cu}$. All snapshots are colored in the same way as Fig. 11.
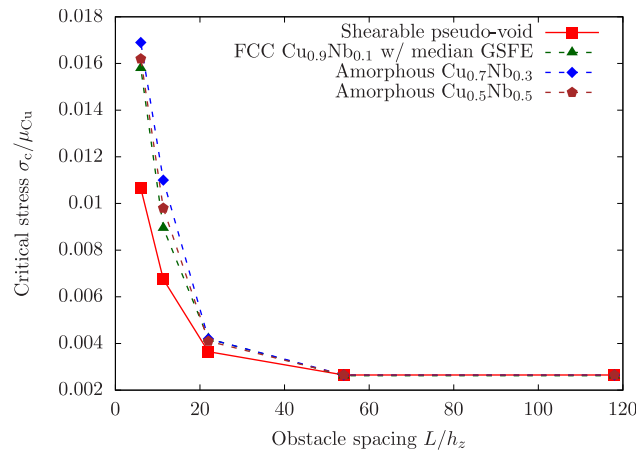

Fig. 18. In a Cu matrix, critical dislocation bypass stress as a function of the obstacle spacing L in the cases of pseudo-voids, $Cu_{0.7}Nb_{0.3}$ amorphous precipitates, $Cu_{0.5}Nb_{0.5}$ amorphous precipitates, and FCC $Cu_{0.9}Nb_{0.1}$ crystalline precipitates with the median GSFE surface.

6.3.1. Amorphous precipitates in a Cu matrix

Selected snapshots for a dislocation bypassing six $Cu_{0.5}Nb_{0.5}$ amorphous precipitates when $L = 11.3h_z$ are presented in Fig. 17. The applied stress in this case is slightly above the threshold value for the dislocation to overcome the array. Since these precipitates are impenetrable by the dislocation, the dislocation is expected to bow around the precipitates rather than cutting them. The bypass of both leading and trailing partial dislocations follows the Orowan mechanism, in which a shear loop is left around the precipitate after both partials glide away.

Fig. 18 compares σ_c for an edge dislocation in Cu to bypass an array of $Cu_{0.7}Nb_{0.3}$ and $Cu_{0.5}Nb_{0.5}$ precipitates for a range of L. As with pseudo-voids and crystalline precipitates, σ_c increases with a decreasing L. Similar to other obstacles, effects of any differences in precipitate properties emerge only for fine spacing $L \leq 22h_z$. Between the two amorphous precipitates, those made of $Cu_{0.7}Nb_{0.3}$ require a higher σ_c for dislocation bypass than those made of $Cu_{0.5}Nb_{0.5}$. The differences in their σ_c are within 5% for $L = 6h_z$, a consequence of small differences in their isotropic shear moduli: $Cu_{0.7}Nb_{0.3}$ has a slightly lower shear moduli (29 GPa) than $Cu_{0.5}Nb_{0.5}$ (30 GPa). As a result, the former has a slightly greater shear modulus mismatch with respect to the matrix Cu (55 GPa). These results suggest that the higher strengthening in $Cu_{0.7}Nb_{0.3}$ arises from a large shear modulus mismatch.

The strengthening by amorphous precipitates can be compared to those in pseudo-voids or crystalline precipitates of the same size and spacing. For the latter two types of obstacles, an important distinction is the bypass mechanism, i.e., the dislocation can eventually cut through the pseudo-voids and crystalline precipitates rather than bowing
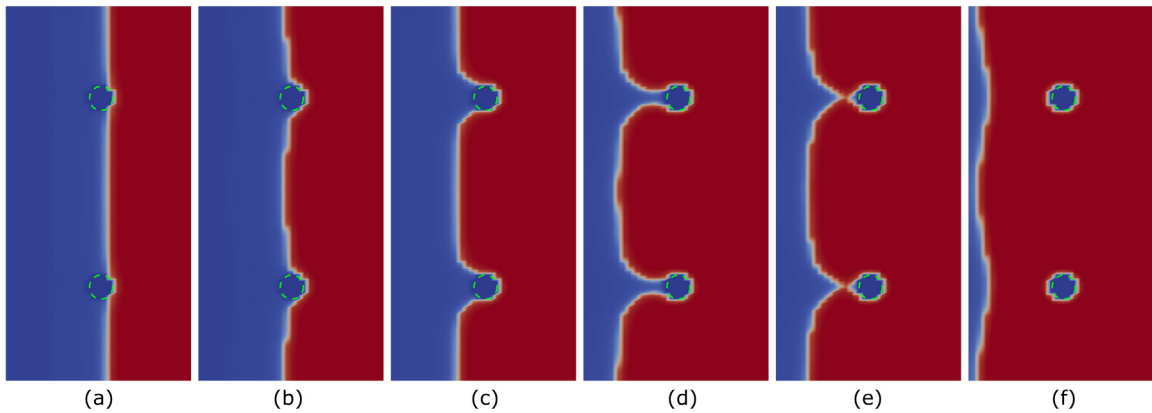
Fig. 19. Snapshots of selected configurations for an edge dislocation bypassing two amorphous $Cu_{0.5}Nb_{0.5}$ precipitates in a Nb matrix. The precipitate spacing $L = 54h_z$. The applied stress is constant and is slightly higher than the critical stress, $0.03595\mu_{Nb}$. All snapshots are colored in the same way as Fig. 11.
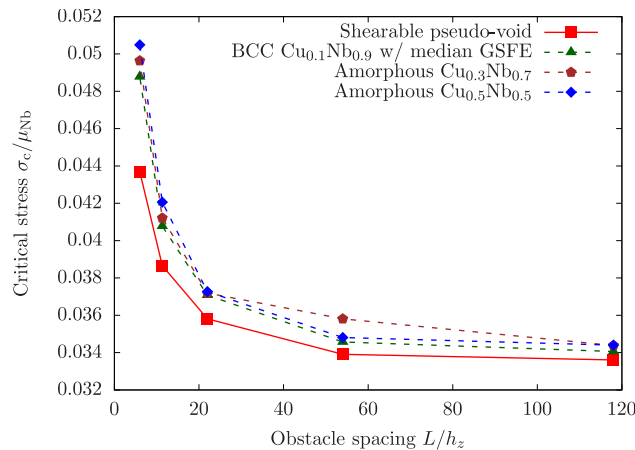

Fig. 20. In a Nb matrix, critical dislocation bypass stress as a function of the obstacle spacing L in the cases of pseudo-voids, $Cu_{0.5}Nb_{0.5}$ amorphous precipitates, $Cu_{0.3}Nb_{0.7}$ amorphous precipitates, and BCC $Cu_{0.1}Nb_{0.9}$ crystalline precipitates with the median GSFE curve.

entirely around them. Consequently, among all obstacles studied, the amorphous precipitates present the highest resistance to bypass. Fig. 18 shows for comparison σ_c for FCC $Cu_{0.9}Nb_{0.1}$ precipitates with the median GSFE surface and pseudo-voids in same matrix Cu. σ_c for either amorphous precipitate are still higher. When $L = 6h_z$, for example, σ_c for the $Cu_{0.5}Nb_{0.5}$ amorphous precipitates is 7% and 59% higher than those for the $Cu_{0.9}Nb_{0.1}$ crystalline precipitates and pseudo-voids, respectively.

6.3.2. Amorphous precipitates in a Nb matrix

Finally, we examine the interaction of an edge dislocation in Nb with amorphous precipitates. For the example shown in Fig. 19, the applied stress is slightly above the threshold σ_c needed for this dislocation to bypass two precipitates. As when this same precipitate lies in a Cu matrix, the dislocation bypasses these amorphous $Cu_{0.5}Nb_{0.5}$ precipitates following the Orowan mechanism, in which it bows between neighboring precipitates, leaving a shear loop around each one.

Fig. 20 presents the variation in σ_c with L for two compositions of amorphous precipitates in Nb: $Cu_{0.5}Nb_{0.5}$ and $Cu_{0.3}Nb_{0.7}$. Compared with the Cu matrix, the effects of modulus differences on σ_c among the unshearable amorphous precipitates in the Nb matrix are more noticeable. Between the two types of amorphous precipitates, $Cu_{0.5}Nb_{0.5}$ requires a higher σ_c for dislocation bypass than those made of $Cu_{0.3}Nb_{0.7}$. Note that $Cu_{0.5}Nb_{0.5}$ precipitate

has a much lower shear modulus than $Cu_{0.3}Nb_{0.7}$ (30 GPa vs. 37 GPa) and hence a much greater shear modulus mismatch with respect to Nb (40 GPa). As seen before in the Cu matrix, the precipitate having a higher modulus mismatch with the matrix is a better strengthener. A similar trend was reported in recent DDD simulations [73].

As a result of the shear loop formation around the precipitates, the amorphous precipitates are much stronger barriers to dislocation glide than crystalline precipitates. For the same range of L, Fig. 20 includes also σ_c for the crystalline $Cu_{0.1}Nb_{0.9}$ precipitates and pseudo-voids of the same size in the same Nb matrix. When $L = 6h_z$, for instance, σ_c for the $Cu_{0.5}Nb_{0.5}$ amorphous precipitates is 4% and 16% higher than those for the $Cu_{0.1}Nb_{0.9}$ crystalline precipitates with the median GSFE curve and pseudo-voids, respectively.

7. Conclusions

In this work, we develop a PFDD model that takes into account elastic heterogeneity, elastic anisotropy, and dissociated dislocations. Dislocations are able to glide in each phase as well as transmit across coherent boundaries between two crystalline phases. The model is applied to study the in-plane interactions between a gliding edge dislocation and an array of obstacles with different spacings in either an FCC Cu or a BCC Nb matrix. For the obstacles, we consider both voids and crystalline or amorphous precipitates. The precipitates are binary alloys, varying in composition, $Cu_{1-x}Nb_x$, where x varies from 0.1 to 0.9. We quantify the effects of obstacle spacing and composition on the critical stresses for the dislocation bypass. The main findings of this study are as follows:

- Using atomistic simulations, we identify the stable phase of the random binary $Cu_{1-x}Nb_x$ as x increases, finding that it ranges from FCC to amorphous and to BCC. We calculate the elastic moduli for all structures, and specifically for the crystalline structures, their lattice parameters and GSFEs.
- All atomistic simulations have shown that the voids are shearable by dislocations. Yet in prior PF dislocation models, the voids were unshearable. We develop a model for shearable pseudo-voids in our PFDD framework. We show that, for the same void spacing and in the same matrix material, the critical stress for a dislocation bypassing pseudo-voids is lower than that for unshearable voids.
- Compared with pseudo-voids, shearable crystalline precipitates are stronger barriers to dislocation glide. In the same matrix material and for the same precipitate spacing, crystalline precipitates with higher GSFEs are stronger obstacles.
- Compared with the crystalline precipitates, the amorphous precipitates are unshearable and are bypassed by a dislocation following the Orowan mechanism, leaving behind a shear loop around the precipitates.
- As a result, among all obstacles studied in this work, amorphous precipitates are the strongest barriers to dislocation motion. Our simulation shows that unshearable precipitates with a larger elastic mismatch with respect to the matrix impede dislocation glide more than those with a smaller elastic mismatch. To best strengthen a material, amorphous precipitates with a larger elastic mismatch with respect to the matrix should be introduced.

Declaration of competing interest

The authors declare that they have no known competing financial interests or personal relationships that could have appeared to influence the work reported in this paper.

Acknowledgments

Appendix A. Derivation of Eq. (16)

Substituting Eqs. (11) and (15) into Eq. (7) yields

$$
\begin{aligned}
\psi_{\text{ela}}(\boldsymbol{x}) &= \frac{1}{2} C_{ijkl}(\boldsymbol{x})[\epsilon_{ij}(\boldsymbol{x}) - \epsilon_{ij}^{\text{p}}(\boldsymbol{x})][\epsilon_{kl}(\boldsymbol{x}) - \epsilon_{kl}^{\text{p}}(\boldsymbol{x})] \\
&= \frac{1}{2}[C_{ijkl}^{[1]} + \Delta C_{ijkl}(\boldsymbol{x})][\epsilon_{ij}(\boldsymbol{x}) - \epsilon_{ij}^{0}(\boldsymbol{x}) + \epsilon_{ij}^{\text{v}}(\boldsymbol{x})][\epsilon_{kl}(\boldsymbol{x}) - \epsilon_{kl}^{0}(\boldsymbol{x}) + \epsilon_{kl}^{\text{v}}(\boldsymbol{x})] \\
&= \frac{1}{2} C_{ijkl}^{[1]}[\epsilon_{ij}(\boldsymbol{x}) - \epsilon_{ij}^{0}(\boldsymbol{x}) + \epsilon_{ij}^{\text{v}}(\boldsymbol{x})][\epsilon_{kl}(\boldsymbol{x}) - \epsilon_{kl}^{0}(\boldsymbol{x}) + \epsilon_{kl}^{\text{v}}(\boldsymbol{x})] \\
&\quad + \frac{1}{2} \Delta C_{ijkl}(\boldsymbol{x})[\epsilon_{ij}(\boldsymbol{x}) - \epsilon_{ij}^{0}(\boldsymbol{x}) + \epsilon_{ij}^{\text{v}}(\boldsymbol{x})][\epsilon_{kl}(\boldsymbol{x}) - \epsilon_{kl}^{0}(\boldsymbol{x}) + \epsilon_{kl}^{\text{v}}(\boldsymbol{x})] \\
&= \frac{1}{2} C_{ijkl}^{[1]}[\epsilon_{ij}(\boldsymbol{x}) - \epsilon_{ij}^{0}(\boldsymbol{x})][\epsilon_{kl}(\boldsymbol{x}) - \epsilon_{kl}^{0}(\boldsymbol{x})] + \frac{1}{2} C_{ijkl}^{[1]}[\epsilon_{ij}(\boldsymbol{x}) - \epsilon_{ij}^{0}(\boldsymbol{x})]\epsilon_{kl}^{\text{v}}(\boldsymbol{x}) \\
&\quad + \frac{1}{2} C_{ijkl}^{[1]}\epsilon_{ij}^{\text{v}}(\boldsymbol{x})[\epsilon_{kl}(\boldsymbol{x}) - \epsilon_{kl}^{0}(\boldsymbol{x}) + \epsilon_{kl}^{\text{v}}(\boldsymbol{x})] \\
&\quad + \frac{1}{2} \Delta C_{ijkl}(\boldsymbol{x})[\epsilon_{ij}(\boldsymbol{x}) - \epsilon_{ij}^{0}(\boldsymbol{x}) + \epsilon_{ij}^{\text{v}}(\boldsymbol{x})][\epsilon_{kl}(\boldsymbol{x}) - \epsilon_{kl}^{0}(\boldsymbol{x}) + \epsilon_{kl}^{\text{v}}(\boldsymbol{x})] \quad\text{(A.1)}
\end{aligned}
$$

There are four terms. The first term is $\psi_{\text{ela}}^{\text{eq}}(\boldsymbol{x})$, according to Eq. (17).
Then, taking advantage of Eq. (13) and the identity $C_{mnij} C_{ijkl}^{-1} = \delta_{mk}\delta_{nl}$, we re-write the second term as

$$
\begin{aligned}
&\frac{1}{2} C_{ijkl}^{[1]}[\epsilon_{ij}(\boldsymbol{x}) - \epsilon_{ij}^{0}(\boldsymbol{x})]\epsilon_{kl}^{\text{v}}(\boldsymbol{x}) \\
&= \frac{1}{2} C_{ijkl}^{[1]}[\epsilon_{ij}(\boldsymbol{x}) - \epsilon_{ij}^{\text{p}}(\boldsymbol{x}) - \epsilon_{ij}^{\text{v}}(\boldsymbol{x})]\epsilon_{kl}^{\text{v}}(\boldsymbol{x}) \\
&= \frac{1}{2} C_{ijkl}^{[1]}[\epsilon_{ij}(\boldsymbol{x}) - \epsilon_{ij}^{\text{p}}(\boldsymbol{x})]\epsilon_{kl}^{\text{v}}(\boldsymbol{x}) - \frac{1}{2} C_{ijkl}^{[1]}\epsilon_{ij}^{\text{v}}(\boldsymbol{x})\epsilon_{kl}^{\text{v}}(\boldsymbol{x}) \\
&= \frac{1}{2} C_{ijkl}^{[1]}[\epsilon_{kl}(\boldsymbol{x}) - \epsilon_{kl}^{\text{p}}(\boldsymbol{x})]\epsilon_{ij}^{\text{v}}(\boldsymbol{x}) - \frac{1}{2} C_{ijkl}^{[1]}\epsilon_{ij}^{\text{v}}(\boldsymbol{x})\epsilon_{kl}^{\text{v}}(\boldsymbol{x}) \\
&= \frac{1}{2} C_{ijmn}^{[1]}\delta_{mk}\delta_{nl}[\epsilon_{kl}(\boldsymbol{x}) - \epsilon_{kl}^{\text{p}}(\boldsymbol{x})]\epsilon_{ij}^{\text{v}}(\boldsymbol{x}) - \frac{1}{2} C_{ijkl}^{[1]}\epsilon_{ij}^{\text{v}}(\boldsymbol{x})\epsilon_{kl}^{\text{v}}(\boldsymbol{x}) \\
&= \frac{1}{2} C_{ijmn}^{[1]} \left[\Delta C_{mnpq}(\boldsymbol{x})\right]^{-1} \Delta C_{pqkl}(\boldsymbol{x})[\epsilon_{kl}(\boldsymbol{x}) - \epsilon_{kl}^{\text{p}}(\boldsymbol{x})]\epsilon_{ij}^{\text{v}}(\boldsymbol{x}) - \frac{1}{2} C_{ijkl}^{[1]}\epsilon_{ij}^{\text{v}}(\boldsymbol{x})\epsilon_{kl}^{\text{v}}(\boldsymbol{x}) \\
&= \frac{1}{2} C_{ijmn}^{[1]} \left[\Delta C_{mnpq}(\boldsymbol{x})\right]^{-1} [-C_{pqkl}^{[1]}\epsilon_{kl}^{\text{v}}(\boldsymbol{x})]\epsilon_{ij}^{\text{v}}(\boldsymbol{x}) - \frac{1}{2} C_{ijkl}^{[1]}\epsilon_{ij}^{\text{v}}(\boldsymbol{x})\epsilon_{kl}^{\text{v}}(\boldsymbol{x}) \\
&= -\frac{1}{2} C_{ijmn}^{[1]} \left[\Delta C_{mnpq}(\boldsymbol{x})\right]^{-1} C_{pqkl}^{[1]}\epsilon_{ij}^{\text{v}}(\boldsymbol{x})\epsilon_{kl}^{\text{v}}(\boldsymbol{x}) - \frac{1}{2} C_{ijkl}^{[1]}\epsilon_{ij}^{\text{v}}(\boldsymbol{x})\epsilon_{kl}^{\text{v}}(\boldsymbol{x}) \\
&= \frac{1}{2} M_{ijkl}(\boldsymbol{x})\epsilon_{ij}^{\text{v}}(\boldsymbol{x})\epsilon_{kl}^{\text{v}}(\boldsymbol{x}) \quad\text{(A.2)}
\end{aligned}
$$

which is $\psi_{\text{ela}}^{\text{ex}}(\boldsymbol{x})$, according to Eq. (18). Substituting Eq. (13) into the third term and considering the symmetry of the elastic tensor yield

$$
\begin{aligned}
&\frac{1}{2} C_{ijkl}^{[1]}\epsilon_{ij}^{\text{v}}(\boldsymbol{x})[\epsilon_{kl}(\boldsymbol{x}) - \epsilon_{kl}^{0}(\boldsymbol{x}) + \epsilon_{kl}^{\text{v}}(\boldsymbol{x})] \\
&= \frac{1}{2} C_{klij}^{[1]}\epsilon_{ij}^{\text{v}}(\boldsymbol{x})[\epsilon_{kl}(\boldsymbol{x}) - \epsilon_{kl}^{0}(\boldsymbol{x}) + \epsilon_{kl}^{\text{v}}(\boldsymbol{x})] \\
&= -\frac{1}{2} \Delta C_{klij}(\boldsymbol{x})[\epsilon_{ij}(\boldsymbol{x}) - \epsilon_{ij}^{\text{p}}(\boldsymbol{x})][\epsilon_{kl}(\boldsymbol{x}) - \epsilon_{kl}^{0}(\boldsymbol{x}) + \epsilon_{kl}^{\text{v}}(\boldsymbol{x})] \\
&= -\frac{1}{2} \Delta C_{ijkl}(\boldsymbol{x})[\epsilon_{ij}(\boldsymbol{x}) - \epsilon_{ij}^{0}(\boldsymbol{x}) + \epsilon_{ij}^{\text{v}}(\boldsymbol{x})][\epsilon_{kl}(\boldsymbol{x}) - \epsilon_{kl}^{0}(\boldsymbol{x}) + \epsilon_{kl}^{\text{v}}(\boldsymbol{x})] \quad\text{(A.3)}
\end{aligned}
$$
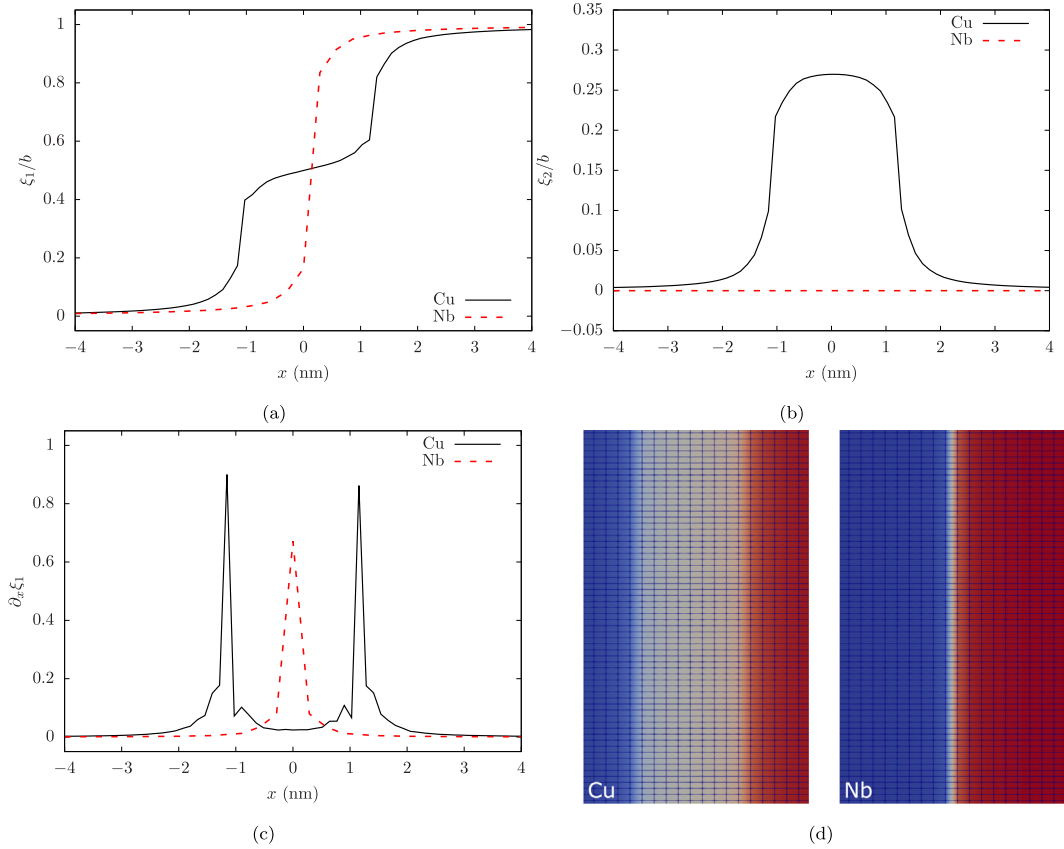
which then cancels out the fourth term.

Fig. B.1. Disregistry fields of an edge dislocation (a) along and (b) normal to the perfect dislocation Burgers vector direction in Cu and Nb. (c) Density of the disregistry field ξ_1 in (a). (d) Snapshots of the equilibrium, stress-free structure of the edge dislocation in Cu (dissociated) and in Nb (undissociated). The in plane numerical grid is also shown. Both snapshots are colored in the same way as Fig. 11.

Therefore,

$$\psi_{\text{ela}}(\boldsymbol{x}) = \psi_{\text{ela}}^{\text{eq}}(\boldsymbol{x}) + \psi_{\text{ela}}^{\text{ex}}(\boldsymbol{x}) \tag{A.4}$$

which is Eq. (16).

Appendix B. Static dislocations and Peierls stresses

For reference, we present the structure of the edge dislocation under stress-free conditions in Cu and Nb. Fig. B.1(a,b) shows the profiles of the disregistry ξ_1 and ξ_2 (Eq. (38)), which are along (ξ_1) and normal (ξ_2) to the perfect dislocation Burgers direction, respectively. Using contours, Fig. B.1(d) shows the disregistry fields for these dislocations, where blue and red correspond to $\xi_1 = 0$ (no slip) and b (slipped), respectively. Light gray corresponds to values of ξ_1 that lie in-between 0 and b and indicates the dislocation. For Cu, the edge dislocation has dissociated into two Shockley partials with a stacking fault inbetween. Fig. B.1(c) presents the disregistry density field $\partial_x \xi_1$, which has two peaks in Cu, each corresponding to a Shockley partial core. The distance between the two peaks is the intrinsic stacking fault width, which is 2.31 nm. For Nb, the dislocation is compact and $\partial_x \xi_1$ shows a single peak.

Next, as another important reference value, we calculate the Peierls stress σ_P of an edge dislocation in either Cu or Nb. In an obstacle-free glide plane, the applied stress is incremented in $10^{-4}\mu$ until the dislocation dipole starts to move. We find that $\sigma_P = 0.00255\mu_{\text{Cu}}$ and $0.03355\mu_{\text{Nb}}$ in Cu and Nb, respectively. Substituting for $\mu_{\text{Cu}} = 54.58$ GPa and $\mu_{\text{Nb}} = 39.64$ GPa (Table 2), $\sigma_P = 139.18$ MPa in Cu and 1329.92 MPa in Nb. Atomistic simulations for Cu

reported σ_P = 3 MPa [56], 2.5 MPa [74], 1.4 MPa [75], and 1.3 MPa [76] for the edge dislocation on the {111} plane, where variations can arise due to differences in simulation cell design and interatomic potentials. Similarly, the Peierls stress of an edge dislocation on the {110} plane in Nb has been determined to be σ_P = 118 MPa [56], 29 MPa [77], 23 MPa [63], and 6 MPa [78], in atomistic simulations. Note the Peierls stress is sensitive to the details of the atomic core and the PFDD model could be augmented to yield more accurate Peierls stresses [79]. In this work, we use our calculated values of σ_P solely as a reference to gauge the resistances of various obstacles to dislocation glide.

References

[1] D.F. Pedraza, A. Card, Irradiation-induced crystalline to amorphous transition in intermetallic compounds. mechanisms and modeling, Radiat. Eff. Defects Solids 129 (1–2) (1994) 99–104, http://dx.doi.org/10.1080/10420159408228885.

[2] S.Z. Xu, Z.M. Hao, Y.Q. Su, W.J. Hu, Y. Yu, Q. Wan, Atomic collision cascades on void evolution in vanadium, Radiat. Eff. Defects Solids 167 (1) (2012) 12–25, http://dx.doi.org/10.1080/10420150.2011.613393.

[3] J.E. Schoutens, Simple and precise measurements of fibre volume and void fractions in metal matrix composite materials, J. Mater. Sci. 19 (3) (1984) 957–964, http://dx.doi.org/10.1007/BF00540466.

[4] Z. Wang, K. Georgarakis, K.S. Nakayama, Y. Li, A.A. Tsarkov, G. Xie, D. Dudina, D.V. Louzguine-Luzgin, A.R. Yavari, Microstructure and mechanical behavior of metallic glass fiber-reinforced Al alloy matrix composites, Sci. Rep. 6 (1) (2016) 24384, http://dx.doi.org/10.1038/srep24384, URL https://www.nature.com/articles/srep24384.

[5] T. Hatano, Dynamics of a dislocation bypassing an impenetrable precipitate: The Hirsch mechanism revisited, Phys. Rev. B 74 (2) (2006) 020102, http://dx.doi.org/10.1103/PhysRevB.74.020102, URL http://link.aps.org/doi/10.1103/PhysRevB.74.020102.

[6] D.J. Bacon, Y.N. Osetsky, Mechanisms of hardening due to copper precipitates in α-iron, Phil. Mag. 89 (34–36) (2009) 3333–3349, http://dx.doi.org/10.1080/14786430903271377.

[7] K.H. Westmacott, R.E. Smallman, P.S. Dobson, The annealing of voids in quenched aluminium and a determination of the surface energy, Metal Sci. J. 2 (1) (1968) 177–181, http://dx.doi.org/10.1179/030634568790443530.

[8] A.J.E. Foreman, M.J. Makin, Dislocation movement through random arrays of obstacles, Phil. Mag. 14 (131) (1966) 911–924, http://dx.doi.org/10.1080/14786436608244762.

[9] H.J. Frost, M.F. Ashby, Motion of a dislocation acted on by a viscous drag through an array of discrete obstacles, J. Appl. Phys. 42 (13) (1971) 5273–5279, http://dx.doi.org/10.1063/1.1659936, URL https://aip.scitation.org/doi/10.1063/1.1659936.

[10] A. Dutta, M. Bhattacharya, N. Gayathri, G.C. Das, P. Barat, The mechanism of climb in dislocation-nanovoid interaction, Acta Mater. 60 (9) (2012) 3789–3798, http://dx.doi.org/10.1016/j.actamat.2012.03.050, URL http://www.sciencedirect.com/science/article/pii/S1359645412002406.

[11] W.-R. Jian, M. Zhang, S. Xu, I.J. Beyerlein, Atomistic simulations of dynamics of an edge dislocation and its interaction with a void in copper: a comparative study, Modelling Simul. Mater. Sci. Eng. 28 (4) (2020) 045004.

[12] L. Xiong, S. Xu, D.L. McDowell, Y. Chen, Concurrent atomistic-continuum simulations of dislocation-void interactions in fcc crystals, Int. J. Plast. 65 (2015) 33–42, http://dx.doi.org/10.1016/j.ijplas.2014.08.002, URL http://www.sciencedirect.com/science/article/pii/S0749641914001508.

[13] S. Xu, D.L. McDowell, I.J. Beyerlein, Sequential obstacle interactions with dislocations in a planar array, Acta Mater. 174 (2019) 160–172, http://dx.doi.org/10.1016/j.actamat.2019.05.030, URL http://www.sciencedirect.com/science/article/pii/S135964541930312X.

[14] R. Santos-Güemes, G. Esteban-Manzanares, I. Papadimitriou, J. Segurado, L. Capolungo, J. LLorca, Discrete dislocation dynamics simulations of dislocation-θ' precipitate interaction in Al-Cu alloys, J. Mech. Phys. Solids 118 (2018) 228–244, http://dx.doi.org/10.1016/j.jmps.2018.05.015, URL https://www.sciencedirect.com/science/article/pii/S0022509617310037.

[15] M.R. Barnett, H. Wang, T. Guo, An Orowan precipitate strengthening equation for mechanical twinning in Mg, Int. J. Plast. 112 (2019) 108–122, http://dx.doi.org/10.1016/j.ijplas.2018.08.010, URL https://www.sciencedirect.com/science/article/pii/S0749641918303231.

[16] Y. Xiang, D.J. Srolovitz, L.T. Cheng, W. E, Level set simulations of dislocation-particle bypass mechanisms, Acta Mater. 52 (7) (2004) 1745–1760, http://dx.doi.org/10.1016/j.actamat.2003.12.016, URL http://www.sciencedirect.com/science/article/pii/S1359645403007651.

[17] Y. Xiang, D.J. Srolovitz, Dislocation climb effects on particle bypass mechanisms, Phil. Mag. 86 (25–26) (2006) 3937–3957, http://dx.doi.org/10.1080/14786430600575427.

[18] T. Tsuru, D.C. Chrzan, Effect of solute atoms on dislocation motion in Mg: An electronic structure perspective, Sci. Rep. 5 (1) (2015) 8793, http://dx.doi.org/10.1038/srep08793, URL https://www.nature.com/articles/srep08793.

[19] Y. Wang, J. Li, Phase field modeling of defects and deformation, Acta Mater. 58 (2010) 1212–1235.

[20] L.-Q. Chen, Phase-field models for microstructure evolution, Annu. Rev. Mater. Res. 32 (1) (2002) 113–140, http://dx.doi.org/10.1146/annurev.matsci.32.112001.132041.

[21] I. Steinbach, Phase-field models in materials science, Modelling Simul. Mater. Sci. Eng. 17 (7) (2009) 073001, http://dx.doi.org/10.1088/0965-0393/17/7/073001.

[22] Y.U. Wang, Y.M. Jin, A.M. Cuitiño, A.G. Khachaturyan, Nanoscale phase field microelasticity theory of dislocations: model and 3D simulations, Acta Mater. 49 (10) (2001) 1847–1857, http://dx.doi.org/10.1016/S1359-6454(01)00075-1, URL http://www.sciencedirect.com/science/article/pii/S1359645401000751.

[23] C. Shen, Y. Wang, Phase field model of dislocation networks, Acta Mater. 51 (9) (2003) 2595–2610, http://dx.doi.org/10.1016/S1359-6454(03)00058-2, URL http://www.sciencedirect.com/science/article/pii/S1359645403000582.

[24] S. Zheng, D. Zheng, Y. Ni, L. He, Improved phase field model of dislocation intersections, npj Comput. Mater. 4 (2018) 20, http://dx.doi.org/10.1038/s41524-018-0075-x, URL https://www.nature.com/articles/s41524-018-0075-x.

[25] C. Shen, Y. Wang, Incorporation of γ-surface to phase field model of dislocations: simulating dislocation dissociation in fcc crystals, Acta Mater. 52 (2004) 683–691.

[26] J.R. Mianroodi, B. Svendsen, Atomistically determined phase field modeling of dislocation dissociation, stacking fault formation, dislocation slip, and reactions in fcc systems, J. Mech. Phys. Solids 77 (2015) 109–122.

[27] C. Shen, J. Li, Y. Wang, Predicting structure and energy of dislocations and grain boundaries, Acta Mater. 74 (2014) 125–131, http://dx.doi.org/10.1016/j.actamat.2014.03.065, URL http://www.sciencedirect.com/science/article/pii/S135964541400233X.

[28] M. Koslowski, A.M. Cuitiño, M. Ortiz, A phase-field theory of dislocation dynamics, strain hardening and hysteresis in ductile single crystals, J. Mech. Phys. Solids 50 (12) (2002) 2597–2635, http://dx.doi.org/10.1016/S0022-5096(02)00037-6, URL http://www.sciencedirect.com/science/article/pii/S0022509602000376.

[29] S. Xu, L. Smith, J.R. Mianroodi, A. Hunter, B. Svendsen, I.J. Beyerlein, A comparison of different continuum approaches in modeling mixed-type dislocations in Al, Modelling Simul. Mater. Sci. Eng. 27 (7) (2019) 074004, http://dx.doi.org/10.1088/1361-651X/ab2d16.

[30] X. Peng, N. Mathew, I.J. Beyerlein, K. Dayal, A. Hunter, A 3D phase field dislocation dynamics model for body-centered cubic crystals, Comput. Mater. Sci. 171 (2020) 109217, http://dx.doi.org/10.1016/j.commatsci.2019.109217.

[31] S. Xu, Y. Su, L.T.W. Smith, I.J. Beyerlein, Frank-Read source operation in six body-centered cubic refractory metals, J. Mech. Phys. Solids 141 (2020) 104017, http://dx.doi.org/10.1016/j.jmps.2020.104017.

[32] C. Albrecht, A. Hunter, A. Kumar, I.J. Beyerlein, A phase field model for dislocations in hexagonal close packed crystals, J. Mech. Phys. Solids 137 (2020) 103823, http://dx.doi.org/10.1016/j.jmps.2019.103823, URL http://www.sciencedirect.com/science/article/pii/S0022509619306751.

[33] C. Albrecht, A. Kumar, S. Xu, A. Hunter, I.J. Beyerlein, Asymmetric equilibrium core structures of pyramidal II $\langle c + a \rangle$ dislocations in ten hexagonal close packed metals, Phys. Rev. Mater. 5 (2021) 043602, http://dx.doi.org/10.1103/PhysRevMaterials.5.043602, URL https://journals.aps.org/prmaterials/abstract/10.1103/PhysRevMaterials.5.043602.

[34] A. Hunter, F. Saied, C. Le, M. Koslowski, Large-scale 3D phase field dislocation dynamics simulations on high-performance architectures, Int. J. High Perform. Comput. Appl. 25 (2) (2011) 223–235, http://dx.doi.org/10.1177/1094342010382534.

[35] T. Ma, H. Kim, N. Mathew, D.J. Luscher, L. Cao, A. Hunter, Dislocation transmission across $\Sigma 3\{112\}$ incoherent twin boundary: a combined atomistic and phase-field study, Acta Mater. 223 (2022) 117447, http://dx.doi.org/10.1016/j.actamat.2021.117447, URL https://www.sciencedirect.com/science/article/pii/S1359645421008260.

[36] Y. Zeng, X. Cai, M. Koslowski, Effects of the stacking fault energy fluctuations on the strengthening of alloys, Acta Mater. 164 (2019) 1–11, http://dx.doi.org/10.1016/j.actamat.2018.09.066, URL http://www.sciencedirect.com/science/article/pii/S135964541830778X.

[37] L.T.W. Smith, Y. Su, S. Xu, A. Hunter, I.J. Beyerlein, The effect of local chemical ordering on Frank-Read source activation in a refractory multi-principal element alloy, Int. J. Plast. 140 (2020) 102850, http://dx.doi.org/10.1016/j.ijplas.2020.102850, URL http://www.sciencedirect.com/science/article/pii/S0749641920304885.

[38] L. Lei, J.L. Marin, M. Koslowski, Phase-field modeling of defect nucleation and propagation in domains with material inhomogeneities, Modelling Simul. Mater. Sci. Eng. 21 (2) (2013) 025009, http://dx.doi.org/10.1088/0965-0393/21/2/025009, URL http://stacks.iop.org/0965-0393/21/i=2/a=025009.

[39] Y. Zeng, A. Hunter, I.J. Beyerlein, M. Koslowski, A phase field dislocation dynamics model for a bicrystal interface system: An investigation into dislocation slip transmission across cube-on-cube interfaces, Int. J. Plast. 79 (2016) 293–313, http://dx.doi.org/10.1016/j.ijplas.2015.09.001, URL http://www.sciencedirect.com/science/article/pii/S0749641915001473.

[40] S. Xu, J.R. Mianroodi, A. Hunter, B. Svendsen, I.J. Beyerlein, Comparative modeling of the disregistry and Peierls stress for dissociated edge and screw dislocations in Al, Int. J. Plast. (2020) 102689, http://dx.doi.org/10.1016/j.ijplas.2020.102689, URL http://www.sciencedirect.com/science/article/pii/S0749641919303808.

[41] S. Xu, J.R. Mianroodi, A. Hunter, I.J. Beyerlein, B. Svendsen, Phase-field-based calculations of the disregistry fields of static extended dislocations in FCC metals, Phil. Mag. 99 (11) (2019) 1400–1428, http://dx.doi.org/10.1080/14786435.2019.1582850.

[42] A. Hunter, R.F. Zhang, I.J. Beyerlein, The core structure of dislocations and their relationship to the material γ-surface, J. Appl. Phys. 115 (13) (2014) 134314, http://dx.doi.org/10.1063/1.4870462, URL http://aip.scitation.org/doi/10.1063/1.4870462.

[43] S. Xu, Y. Su, I.J. Beyerlein, Modeling dislocations with arbitrary character angle in face-centered cubic transition metals using the phase-field dislocation dynamics method with full anisotropic elasticity, Mech. Mater. 139 (2019) 103200, http://dx.doi.org/10.1016/j.mechmat.2019.103200.

[44] J.D. Eshelby, The determination of the elastic field of an ellipsoidal inclusion, and related problems, Proc. R. Soc. Lond. Ser. A Math. Phys. Eng. Sci. 241 (1226) (1957) 376–396, http://dx.doi.org/10.1098/rspa.1957.0133, URL https://royalsocietypublishing.org/doi/10.1098/rspa.1957.0133.

[45] Y. Ni, M.Y.M. Chiang, Prediction of elastic properties of heterogeneous materials with complex microstructures, J. Mech. Phys. Solids 55 (3) (2007) 517–532, http://dx.doi.org/10.1016/j.jmps.2006.09.001, URL https://www.sciencedirect.com/science/article/pii/S0022509606001360.

[46] Y.M. Jin, Y.U. Wang, A.G. Khachaturyan, Three-dimensional phase field microelasticity theory and modeling of multiple cracks and voids, Appl. Phys. Lett. 79 (19) (2001) 3071–3073, http://dx.doi.org/10.1063/1.1418260, URL https://aip.scitation.org/doi/10.1063/1.1418260.

[47] Y.U. Wang, Y.M. Jin, A.G. Khachaturyan, Phase field microelasticity theory and simulation of multiple voids and cracks in single crystals and polycrystals under applied stress, J. Appl. Phys. 91 (10) (2002) 6435–6451, http://dx.doi.org/10.1063/1.1471389, URL https://aip.scitation.org/doi/10.1063/1.1471389.

[48] Y.U. Wang, Y.M. Jin, A.G. Khachaturyan, Phase field microelasticity modeling of dislocation dynamics near free surface and in heteroepitaxial thin films, Acta Mater. 51 (14) (2003) 4209–4223, http://dx.doi.org/10.1016/S1359-6454(03)00238-6, URL http://www.sciencedirect.com/science/article/pii/S1359645403002386.

[49] K. Doihara, T. Okita, M. Itakura, M. Aichi, K. Suzuki, Atomic simulations to evaluate effects of stacking fault energy on interactions between edge dislocation and spherical void in face-centred cubic metals, Phil. Mag. 98 (22) (2018) 2061–2076, http://dx.doi.org/10.1080/14786435.2018.1472401.

[50] D. Terentyev, D.J. Bacon, Y.N. Osetsky, Interaction of an edge dislocation with voids in α-iron modelled with different interatomic potentials, J. Phys.: Condens. Matter 20 (44) (2008) 445007, http://dx.doi.org/10.1088/0953-8984/20/44/445007.

[51] A. Vaid, J. Guénolé, A. Prakash, S. Korte-Kerzel, E. Bitzek, Atomistic simulations of basal dislocations in Mg interacting with $Mg_{17}Al_{12}$ precipitates, Materialia 7 (2019) 100355, http://dx.doi.org/10.1016/j.mtla.2019.100355, URL http://www.sciencedirect.com/science/article/pii/S2589152919301516.

[52] Y. Su, S. Xu, I.J. Beyerlein, Density functional theory calculations of generalized stacking fault energy surfaces for eight face-centered cubic transition metals, J. Appl. Phys. 126 (10) (2019) 105112, http://dx.doi.org/10.1063/1.5115282, URL https://aip.scitation.org/doi/10.1063/1.5115282.

[53] H. Warlimont, W. Martienssen (Eds.), Springer Handbook of Materials Data, second ed., in: Springer Handbooks, Springer International Publishing, 2018, URL https://www.springer.com/us/book/9783319697413.

[54] S. Plimpton, Fast parallel algorithms for short-range molecular dynamics, J. Comput. Phys. 117 (1) (1995) 1–19, http://dx.doi.org/10.1006/jcph.1995.1039, URL http://www.sciencedirect.com/science/article/pii/S002199918571039X.

[55] L. Zhang, E. Martinez, A. Caro, X.-Y. Liu, M.J. Demkowicz, Liquid-phase thermodynamics and structures in the Cu-Nb binary system, Modelling Simul. Mater. Sci. Eng. 21 (2) (2013) 025005.

[56] W.-R. Jian, Y. Su, S. Xu, W. Ji, I.J. Beyerlein, Effect of interface structure on dislocation glide behavior in nanolaminates, J. Mater. Res. 36 (13) (2021) 2802–2815, http://dx.doi.org/10.1557/s43578-021-00261-y.

[57] J. Xu, S. Xu, I.J. Beyerlein, Atomistic simulations of dipole tilt wall stability in thin films, Thin Solid Films 689 (2019) 137457.

[58] W.-R. Jian, S. Xu, I.J. Beyerlein, On the significance of model design in atomistic calculations of the Peierls stress in Nb, Comput. Mater. Sci. 188 (2021) 110150, http://dx.doi.org/10.1016/j.commatsci.2020.110150, URL http://www.sciencedirect.com/science/article/pii/S0927025620306418.

[59] S. Xu, L. Xiong, Y. Chen, D.L. McDowell, Comparing EAM potentials to model slip transfer of sequential mixed character dislocations across two symmetric tilt grain boundaries in Ni, JOM 69 (5) (2017) 814–821, http://dx.doi.org/10.1007/s11837-017-2302-1, URL https://link.springer.com/article/10.1007/s11837-017-2302-1.

[60] S. Xu, J.K. Startt, T.G. Payne, C.S. Deo, D.L. McDowell, Size-dependent plastic deformation of twinned nanopillars in body-centered cubic tungsten, J. Appl. Phys. 121 (17) (2017) 175101, http://dx.doi.org/10.1063/1.4982754, URL http://aip.scitation.org/doi/10.1063/1.4982754.

[61] A. Zunger, S.-H. Wei, L.G. Ferreira, J.E. Bernard, Special quasirandom structures, Phys. Rev. Lett. 65 (3) (1990) 353–356, http://dx.doi.org/10.1103/PhysRevLett.65.353, URL https://link.aps.org/doi/10.1103/PhysRevLett.65.353.

[62] A. van de Walle, P. Tiwary, M. de Jong, D.L. Olmsted, M. Asta, A. Dick, D. Shin, Y. Wang, L.Q. Chen, Z.K. Liu, Efficient stochastic generation of special quasirandom structures, CALPHAD 42 (2013) 13–18, http://dx.doi.org/10.1016/j.calphad.2013.06.006, URL http://www.sciencedirect.com/science/article/pii/S0364591613000540.

[63] X. Wang, S. Xu, W.-R. Jian, X.-G. Li, Y. Su, I.J. Beyerlein, Generalized stacking fault energies and Peierls stresses in refractory body-centered cubic metals from machine learning-based interatomic potentials, Comput. Mater. Sci. 192 (2021) 110364, http://dx.doi.org/10.1016/j.commatsci.2021.110364, URL https://www.sciencedirect.com/science/article/abs/pii/S0927025621000896.

[64] S. Xu, S.Z. Chavoshi, Y. Su, On calculations of basic structural parameters in multi-principal element alloys using small atomistic models, Comput. Mater. Sci. 202 (2022) 110942, http://dx.doi.org/10.1016/j.commatsci.2021.110942, URL https://www.sciencedirect.com/science/article/pii/S0927025621006406.

[65] A. Stukowski, Visualization and analysis of atomistic simulation data with OVITO—the Open Visualization Tool, Modelling Simul. Mater. Sci. Eng. 18 (1) (2010) 015012, http://dx.doi.org/10.1088/0965-0393/18/1/015012, URL http://iopscience.iop.org/0965-0393/18/1/015012.

[66] C. Michaelsen, C. Gente, R. Bormann, The thermodynamics of amorphous phases in immiscible systems: The example of sputter-deposited Nb-Cu alloys, J. Appl. Phys. 81 (9) (1997) 6024–6030, http://dx.doi.org/10.1063/1.364451, URL https://aip.scitation.org/doi/abs/10.1063/1.364451.

[67] Y. Su, S. Xu, I.J. Beyerlein, *Ab initio*-informed phase-field modeling of dislocation core structures in equal-molar CoNiRu multi-principal element alloys, Modelling Simul. Mater. Sci. Eng. 27 (8) (2019) 084001, http://dx.doi.org/10.1088/1361-651X/ab3b62.

[68] S. Xu, E. Hwang, W.-R. Jian, Y. Su, I.J. Beyerlein, Atomistic calculations of the generalized stacking fault energies in two refractory multi-principal element alloys, Intermetallics 124 (2020) 106844.

[69] R.A. Romero, S. Xu, W.-R. Jian, I.J. Beyerlein, C. Ramana, Atomistic simulations of the local slip resistances in four refractory multi-principal element alloys, Int. J. Plast. 149 (2022) 103157.

[70] M. Bahramyan, R.T. Mousavian, D. Brabazon, Molecular dynamic simulation of edge dislocation-void interaction in pure Al and Al-Mg alloy, Mater. Sci. Eng. A 674 (2016) 82–90, http://dx.doi.org/10.1016/j.msea.2016.07.121, URL http://www.sciencedirect.com/science/article/pii/S0921509316308966.

[71] R.O. Scattergood, D.J. Bacon, The strengthening effect of voids, Acta Metall. 30 (8) (1982) 1665–1677, http://dx.doi.org/10.1016/0001-6160(82)90188-2, URL http://www.sciencedirect.com/science/article/pii/0001616082901882.

[72] J.C. Crone, L.B. Munday, J. Knap, Capturing the effects of free surfaces on void strengthening with dislocation dynamics, Acta Mater. 101 (2015) 40–47, http://dx.doi.org/10.1016/j.actamat.2015.08.067, URL http://www.sciencedirect.com/science/article/pii/S1359645415006540.

[73] B.A. Szajewski, J.C. Crone, J. Knap, Dislocation precipitate bypass through elastically mismatched precipitates, Modelling Simul. Mater. Sci. Eng. 29 (2) (2021) 025005, http://dx.doi.org/10.1088/1361-651X/abd015.

[74] S. Xu, L. Xiong, Y. Chen, D.L. McDowell, An analysis of key characteristics of the Frank-Read source process in FCC metals, J. Mech. Phys. Solids 96 (2016) 460–476, http://dx.doi.org/10.1016/j.jmps.2016.08.002, URL http://www.sciencedirect.com/science/article/pii/S0022509616301016.

[75] G. Liu, X. Cheng, J. Wang, K. Chen, Y. Shen, Peierls stress in face-centered-cubic metals predicted from an improved semi-discrete variation Peierls-Nabarro model, Scr. Mater. 120 (2016) 94–97, http://dx.doi.org/10.1016/j.scriptamat.2016.04.013, URL http://www.sciencedirect.com/science/article/pii/S1359646216301348.

[76] Y. Tang, Uncovering the inertia of dislocation motion and negative mechanical response in crystals, Sci. Rep. 8 (1) (2018) 140.

[77] X.-G. Li, C. Chen, H. Zheng, Y. Zuo, S.P. Ong, Complex strengthening mechanisms in the NbMoTaW multi-principal element alloy, npj Comput. Mater. 6 (2020) 70.

[78] S. Xu, Y. Su, W.-R. Jian, I.J. Beyerlein, Local slip resistances in equal-molar MoNbTi multi-principal element alloy, Acta Mater. 202 (2021) 68–79.

[79] H. Kim, N. Mathew, D.J. Luscher, A. Hunter, Phase field dislocation dynamics (PFDD) modeling of non-Schmid behavior in BCC metals informed by atomistic simulations, J. Mech. Phys. Solids 152 (2021) 104460, http://dx.doi.org/10.1016/j.jmps.2021.104460, URL https://www.sciencedirect.com/science/article/pii/S0022509621001368.